DISCLAIMER

ORNL/TM-2025/4015

Gamma and Neutron Measurement and Modeling of Irradiated TRISO Fuel

Jianwei Hu
Donny Hartanto
Greg Nutter
Ramkumar Venkataraman
Robert McElroy
Callie Goetz

August 2025

OAK RIDGE National Laboratory

ORNL IS MANAGED BY UT-BATTELLE LLC FOR THE US DEPARTMENT OF ENERGY

ORNL/TM-2025/4015

Nuclear Energy and Fuel Cycle Division

GAMMA AND NEUTRON MEASUREMENT AND MODELING OF IRRADIATED TRISO FUEL

Jianwei Hu
Donny Hartanto
Greg Nutter
Ramkumar Venkataraman
Robert McElroy
Callie Goetz

August 2025

Prepared by
OAK RIDGE NATIONAL LABORATORY
Oak Ridge, TN 37831
managed by
UT-BATTELLE LLC
for the
US DEPARTMENT OF ENERGY
under contract DE-AC05-00OR22725

CONTENTS

LIST OF FIGURES

LIST OF TABLES

ABBREVIATIONS

ORNL	Oak Ridge National Laboratory
AGR	Advanced Gas Reactor
ATR	Advanced Test Reactor
CZT	cadmium zinc telluride
DOE	Department of Energy
FHR	fluoride salt-cooled high-temperature reactor
FIMA	fissions per initial metal atom
FWHM	full width at half maximum
HDPE	high-density polyethylene
HFIR	High Flux Isotope Reactor
HPGe	high-purity germanium
IAEA	International Atomic Energy Agency
IFEL	Irradiated Fuels Examination Laboratory
INL	Idaho National Laboratory
KP	Kairos Power
LWR	light water reactor
MCNP	Monte Carlo N-Particle
MC&A	material control and accounting
NSUF	Nuclear Science User Facilities
PBR	pebble bed reactor
PWR	pressurized water reactor
ORNL	Oak Ridge National Laboratory
SEL	Safeguards Extension Laboratory
TRISO	tri-structural isotropic
VPMC	very high-performance neutron multiplicity counter
US	United States

AKNOWLEDGMENT

This work was funded by the National Nuclear Security Administration of the US Department of Energy, Office of Defense Nuclear Nonproliferation Research and Development.

The authors would like to thank Darren Skitt, Tyler Gerczak, Will Cureton, and Jason Harp for providing access to the Advanced Gas Reactor fuel samples. The authors would like to thank Annabelle Le Coq and Kory Linton for providing access to the Kairos Power samples. The authors would like to thank Binh Pham of Idaho National Laboratory for providing access to a subset of the JMOCUP physics depletion calculations results on the Advanced Gas Reactor samples. The authors are also very grateful for all the support provided by John Hinds and his crew at the hot cell.

ABSTRACT

Given the unique characteristics of the pebble bed reactor fuel cycle, both gamma and neutron measurements are expected to play important roles in performing and maintaining nuclear material control and accounting for spent fuel pebbles to safeguard the fuel cycle. Given the lack of irradiated pebbles in the United States, a variety of irradiated TRISO fuel samples with wide ranges of burnups and cooling times, available at Oak Ridge National Laboratory, were used in this work. A large number of gamma and neutron measurements were performed on these samples to collect data to test various detectors and to benchmark computer models used to simulate the depletion and decay of fuels and the measurements themselves. Two neutron detectors, a custom-made detector and the Very High-Performance Neutron Multiplicity Counter, were used to measure the neutrons emitted by these TRISO samples. Three gamma spectrometry detectors, including a high-purity germanium (HPGe) detector, the M400 CZT detector, and a sodium iodide (NaI), were used to measure gamma-ray emissions from these samples. As a room-temperature gamma spectrometer, the M400 was recently adopted by the International Atomic Energy Agency for fresh uranium measurements, but it has not been tested for spent fuel measurements before this project. Detailed Monte Carlo N-Particle (MCNP) models were developed to simulate these neutron and gamma measurements. Some GADRAS models were also developed to cross-check the MCNP models for the gamma measurements. It was found challenging to perform neutron measurements in the hot cell owing to the high background counts. Close agreements were observed between the simulated and measured neutron count rates in both detectors' measurements of californium calibration sources. Both the HPGe and M400 detectors were able to measure the 604 and 662 keV gamma peaks from these samples, which are the two most important peaks used to infer fuel burnup. Although the M400 detector had poorer energy resolution than the HPGe detector and did not detect some of the minor peaks identified by the HPGe detector, it was found to be capable of handling significantly higher dose rates than the HPGe. Given the complexities in the TRISO samples (e.g., different sample sizes) and uncertainties in the alignments between the detector and the TRISO fuel inside the opaque containers, large scatters were found between the peak area rates and the sample burnups. However, the 604/662 peak ratios were found to trend well with the burnups among most samples in both measured and simulated results.

1. INTRODUCTION

Pebble bed reactors (PBRs) are advanced reactor technologies that have received increasing interest and investment from nuclear companies and government agencies worldwide. However, these reactors present unique and complex challenges in nuclear material control and accounting (MC&A) compared with conventional light-water reactors (LWRs). Unlike LWRs, which use a relatively small number of individually identifiable fuel assemblies, PBRs employ hundreds of thousands of small, identical, and unmarked fuel elements known as pebbles. Figure 1 illustrates a typical pebble with a large number of tri-structural isotropic (TRISO) particles embedded in the pebble's graphite matrix. For instance, X-energy's Xe-100 reactor contains approximately 220,000 pebbles circulating continuously through the core [1], as fresh pebbles are introduced, partially burned pebbles recirculated, and spent pebbles permanently removed. This dynamic and continuous operational scheme, as illustrated in Figure 2, significantly complicates existing safeguards approaches such as item-counting, making them impractical or impossible to apply. Additionally, reactor operators frequently measure the burnup of pebbles shortly after their discharge, likely using gamma spectroscopy, to decide whether a pebble should be recirculated or permanently discarded. This process inherently provides regular and direct access to irradiated pebbles containing sensitive nuclear materials like uranium and plutonium. Given these stark differences between the PBR and LWR fuel cycles, the established MC&A approaches used by the International Atomic Energy Agency (IAEA) and other international safeguards authorities do not directly fit the PBR fuel cycle, so new approaches must be developed. Under the sponsorship of the National Nuclear Security Administration of the US Department of Energy (DOE) Office of Defense Nuclear Nonproliferation Research and Development, this project was begun in FY 2023. Its overall goal is to develop an integrated measurement and analysis approach, complemented by data analytics methods, to improve the MC&A of irradiated/spent pebble fuel. Such improvements in MC&A will provide a technical basis for the IAEA and its partners to form an integrated approach to safeguard the PBR fuel cycle.

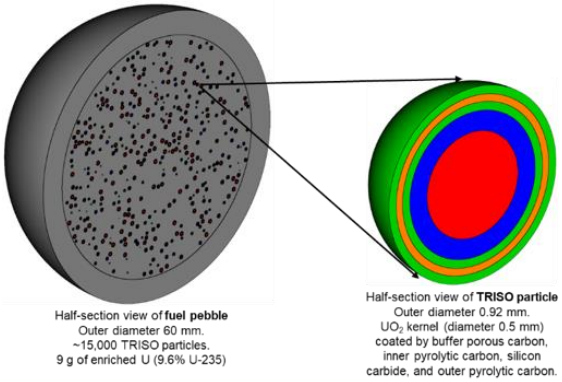

Figure 1. Illustration of a pebble and a TRISO particle.

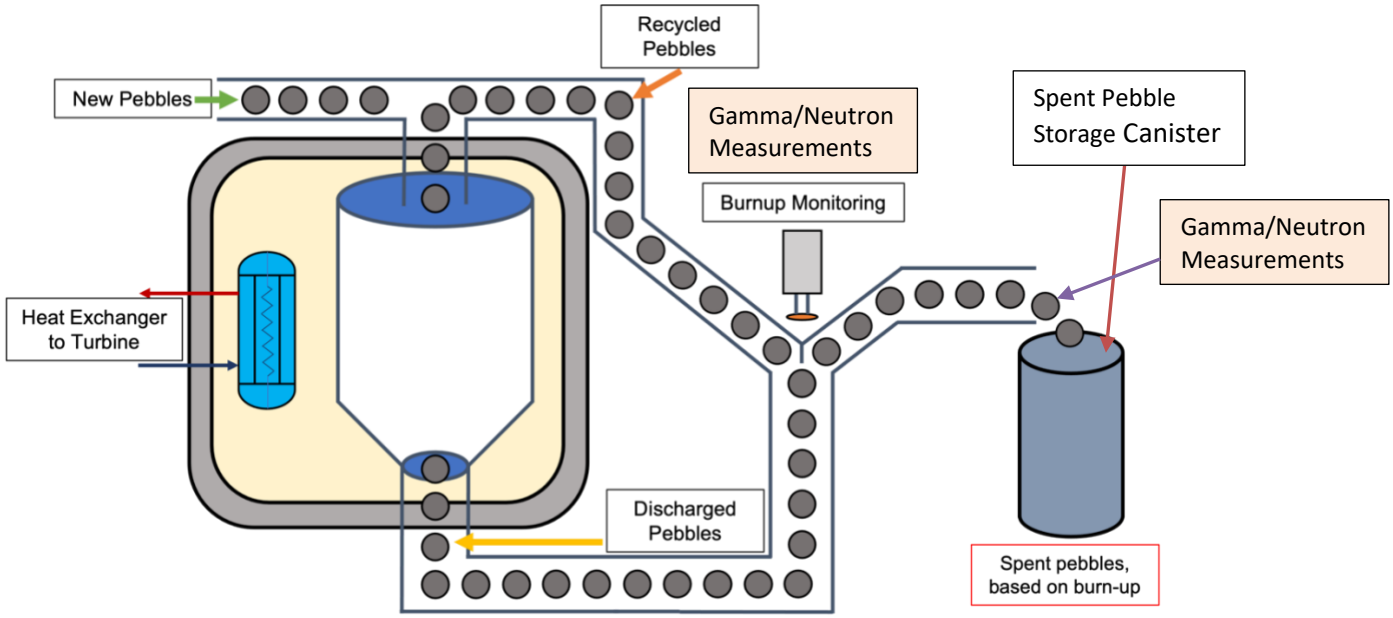

Figure 2. Diagram of the PBR fuel-cycle scheme.

It is expected that gamma and neutron measurements of individual irradiated (or spent pebble when it is fully burned) pebbles will be required for MC&A safeguards purposes, although the IAEA official guidelines for MC&A requirements for PBRs have not been published. The two probable measurement locations are labeled in Figure 2: at the burnup measurement station (as denoted by "Burnup Monitoring" in the figure) and at the inlet of the spent pebble storage canister. The measurement time at the burnup station will likely be limited owing to the large number of pebbles (e.g., 500 pebbles/day in the case of PBMR-400 [2] going through the process each day; whereas only a fraction (e.g., ~1/6) of those pebbles will be directed toward the storage canister, and thus the measurement time at the canister inlet will not be as limited. A PBR operator usually collects the gamma spectrum from a pebble using a gamma spectrometer (e.g., a high-purity germanium [HPGe] detector) to measure the pebble's burnup value. Figure 3 shows the schematic diagram of the burnup measurement system of HTR-10 using an HPGe gamma detector [3].

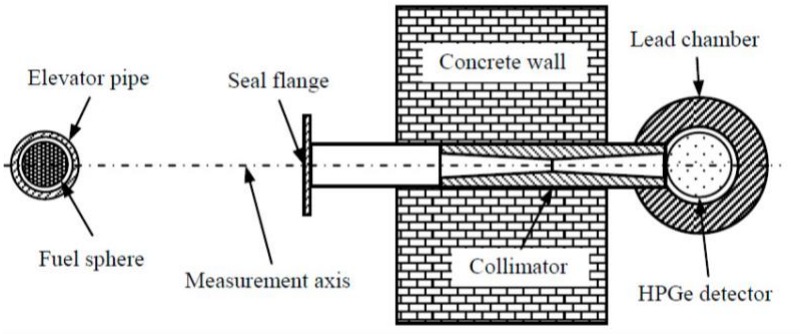

Figure 3. Schematic diagram of the burnup measurement system of HTR-10 [3].

The gamma spectra from an irradiated pebble are dominated by the fission products (e.g., ^{134}Cs, ^{137}Cs, ^{154}Eu) that usually trend linearly with burnup, whereas the focus of MC&A is usually on the U, Pu, and fissile content (e.g., ^{235}U and ^{239}Pu) in the pebble, which can be inferred based on the burnup value determined from the measured gamma spectra. Neutron measurements can complement the gamma

measurements in that (1) the passive neutron measurement signals originate mostly from the spontaneous fission of heavy actinides, notably curium isotopes (^{242}Cm and ^{244}Cm), which trend exponentially with burnup; and (2) the active neutron measurement signals are mostly from induced fissions in the fissile content, which provide a direct measure of a pebble's fissile content. Such neutron measurements can help distinguish pebbles with similar burnups (thus similar gamma spectra) but with different initial enrichments, which is an important capability for safeguards because it can detect potential misuse of a PBR fuel cycle (e.g., using pebbles with lower enrichment to breed Pu). Note that less-enriched pebbles are usually first loaded into the core during the startup of a new PBR before regular pebbles are added to bring the core into equilibrium. In another key task of this project, a neutron detector conceptual design based on differential die-away (DDA) [4, 5, 6] techniques has been developed and investigated to determine the fissile content in irradiated/spent pebbles [7].

In order to collect data to quantify detector performance and to benchmark computer models that are relevant to PBR MC&A applications, a comprehensive effort was recently made in this project to perform a series of gamma and neutron measurements on a select set of irradiated TRISO fuel samples available at Oak Ridge National Laboratory (ORNL). Given that all three of the operating PBRs are located in China, there is no access to irradiated pebbles in the United States. The data from the TRISO samples resemble those expected from pebbles, because a pebble is made of TRISO particles. This report describes these gamma and neutron measurements, the analysis of these measurements, and the modeling of the measurements in the subsequent sections.

Neutron measurements utilized a custom-made neutron detector and the Very High-Performance Neutron Multiplicity Counter (VPMC) [8], which was developed for a previous NNSA project. Gamma-ray measurements were performed using standard HPGe detectors, known for their exceptional energy resolution, alongside advanced M400 cadmium zinc telluride (CZT) detectors valued for their compact design, room-temperature operation, and portability.

The experimental neutron and gamma emission data obtained from these measurement campaigns were compared with the computational models conducted with version 6.2 of the Monte Carlo N-Particle (MCNP) transport code [9].

2. DESCRIPTION OF THE GAMMA AND NEUTRON MEASUREMENTS

2.1 THE IRRADIATED TRISO FUEL SAMPLES

Over the course of this project, we leveraged access to irradiated TRISO fuel samples at ORNL during certain allotted time windows, which were made available by several other DOE projects, to perform the gamma and neutron measurements. The majority of these samples are from the Advanced Gas Reactor (AGR) program [10] [11], which has primarily focused on developing, testing, and qualifying TRISO fuel to accelerate the deployment and commercial viability of high-temperature gas-cooled reactors. The rest of the TRISO samples are provided by the Nuclear Science User Facilities (NSUF) Kairos Power MiniFuel project that primarily studies TRISO fuel performance. To ensure clarity throughout this report, samples from these programs will be referred to as "AGR samples" and "KP samples," respectively. These samples are usually stored in the hot cell of ORNL's Irradiated Fuels Examination Laboratory (IFEL) because of their high gamma dose rates. However, seven individual irradiated AGR TRISO particles were made available by other projects at ORNL's Safeguards Extension Laboratory (SEL), and they were also measured for this project.

The AGR samples were irradiated at Idaho National Laboratory's (INL) Advanced Test Reactor (ATR), and the KP samples were irradiated at ORNL's High Flux Isotope Reactor (HFIR). Table 1 and Table 2 show the list of AGR samples [12] [13] and the KP samples [14], respectively, that were measured at the hot cell in this work and their main characteristics. (The intact TRISO compacts are shown in bold fonts in both tables.) As shown, the AGR list includes two intact TRISO compacts and 13 cans containing loose TRISO particles retrieved from previously irradiated compacts. The KP list includes two intact TRISO compacts along with three partially broken compacts. Table 3 shows the seven individual AGR TRISO particles measured at SEL and their main characteristics. The burnup values shown in these three tables were calculated via reactor physics modeling. The first particle in this table was used in a separate study [15] before this work.

As indicated in Table 1, the majority of the AGR samples originate from the AGR-2 irradiation campaign, and they have significantly longer cooling periods compared with the more recently irradiated AGR-5/6/7 samples [12] [13]. In contrast, the KP samples [14] have relatively shorter cooling times, even compared with the AGR-5/6/7 samples. Additionally, the burnup levels for the AGR samples vary from approximately 70.1 to 137.6 GWd/MTU, while the KP samples have burnups ranging from approximately 19.2 to 119.0 GWd/MTU. The individual particle burnups vary from 72 to 135 GWd/MTU, with most having cooling periods of around 140 months.

The AGR compacts follow prototypical TRISO compact designs, characterized by a cylindrical geometry measuring approximately 1.23 cm in diameter and 2.52 cm in length. Each AGR compact typically contains about 3,000 TRISO particles. By comparison, the KP compacts utilized a smaller, specialized design known as "MiniFuel," measuring approximately 0.46 cm in diameter and 0.305 cm in length, with each compact containing roughly 20 TRISO particles.

Figure 4 shows the collection of AGR samples (listed in Table 1) measured in the hot cell. Except for the two intact compacts, all other AGR samples are stored in stainless steel pellet cans containing loose TRISO particles. Figure 5 shows an AGR compact and its dog-bone-shaped stainless-steel container. It also shows an x-ray radiograph of an AGR compact, which indicates the randomly packed TRISO particles embedded in the graphite matrix. Figure 6 provides pictures of the intact and broken compacts and loose TRISO particles of the measured KP samples; all the KP samples are stored in pellet cans.

Table 1. The list of AGR TRISO fuel samples identified for neutron and gamma measurements for this project and the characteristics of these samples [10] [11] [12] [13].

AGR ID	Type	No. of particles	AGR #	Cooling time (months)	Burnup (GWd/MTU)	UCO or UO_2?	% enrichment
643A	loose particles	~235	2	119	70.1	UCO	14.0
642-03	loose particles	200	2	119	93.1	UCO	14.0
621A	loose particles	~235	2	119	97.9	UCO	14.0
622A	loose particles	~235	2	119	97.9	UCO	14.0
331-03	loose particles	150	2	119	98.9	UO_2	9.6
2-311A	loose particles	~150	2	119	101.8	UO_2	9.6
2-312A	loose particles	~150	2	119	102.7	UO_2	9.6
2-542	loose particles	~2858	2	119	115.2	UCO	14.0
2-521A	loose particles	~235	2	119	118.1	UCO	14.0
212A	loose particles	~235	2	119	121.0	UCO	14.0
2-222-03	loose particles	200	2	119	121.9	UCO	14.0
2-211	**intact compact**	**~3176**	**2**	**119**	120.0	**UCO**	**14.0**
5-222A	loose particles	~235	5/6/7	38	134.4	UCO	15.5
5-224A	loose particles	~235	5/6/7	38	137.3	UCO	15.5
5-159A	loose particles	~235	5/6/7	38	89.3	UCO	15.5
5-223	**intact compact**	**~2265**	**5/6/7**	**38**	137.6	**UCO**	15.5

Table 2. The list of KP TRISO fuel samples identified for neutron and gamma measurements for this project and the characteristics of these samples [14].

Compact ID	Container ID	Comment	No. of particles	% enrichment	Burnup (GWd/MTU)	Cooling time (months)
KP123	50652	broken	17-19	14.0	114.2	22
KP124	50654	broken	17-19	9.6	82.6	22
KP125	50962	broken	17-19	14.0	114.2	22
KP223	**50651**	**intact**	**20**	**14.0**	119.0	**22**
KP224	**50653**	**intact**	**20**	**0.71**	**19.2**	**22**

Table 3. The list of seven individual irradiated AGR TRISO particles measured at SEL and the characteristics of these particles [10].

Particle ID	AGR#	Compact ID	No. of particles	% enrichment	Burnup (GWd/MTU)	Cooling time (months)	Measured gamma dose rate (mR/h)*
RS24 [15]	AGR5/6/7	221	1	15.5	135	37	500
XR136	AGR2	633	1	14	71.6	140	10
D70	AGR2	623	2	14	78.9	140	4.5
XR161	AGR2	642	1	14	88.9	140	9
D10	AGR2	523	1	14	100	140	0.8
XR143	AGR2	541	1	14	115.7	140	14

* Measured by a radiological control technician on contact.

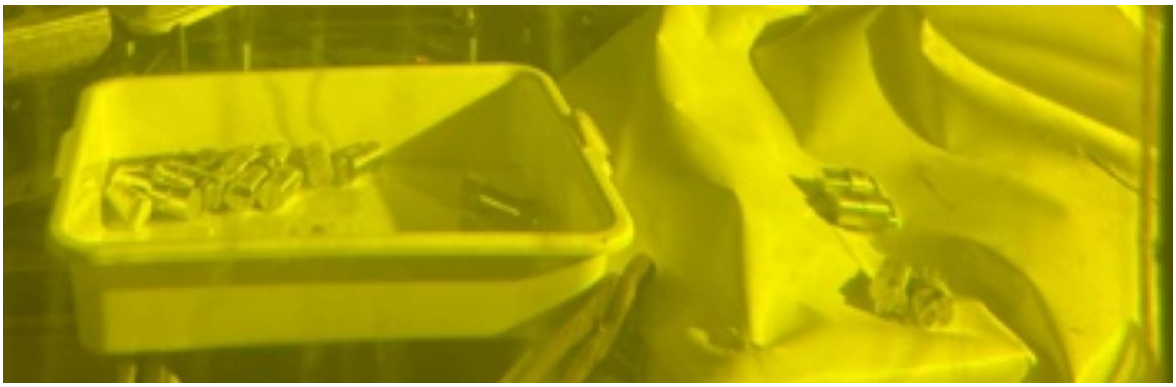

Figure 4. The AGR fuel samples that were available for measurements for this project.

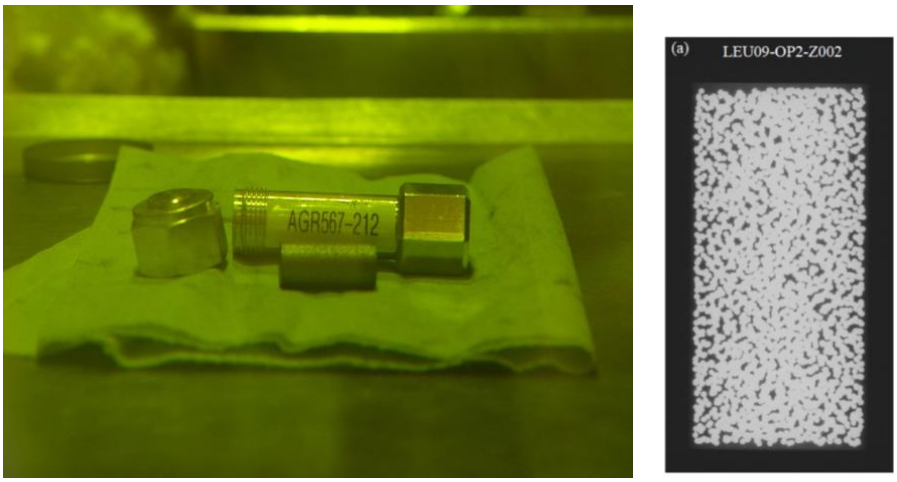

Figure 5. (Left) a photograph of an AGR-5/6/7 compact and its container; (right) an x-ray radiograph of an AGR compact (not to scale). (Note that each white dot in the right figure was a kernel of a TRISO particle.)

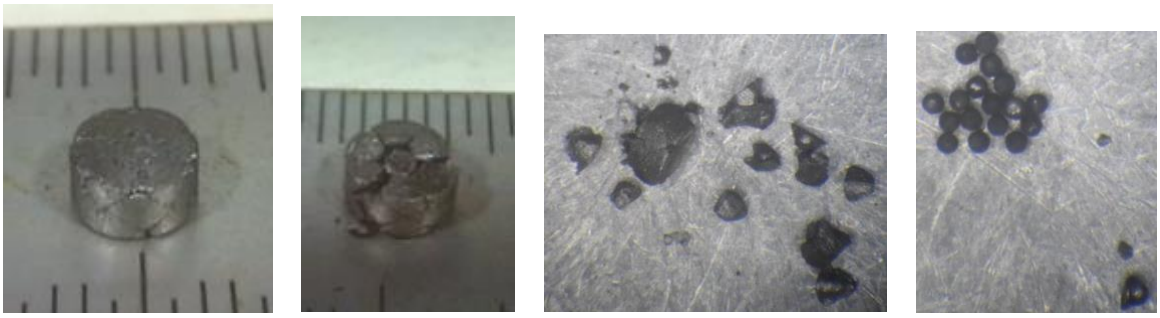

Figure 6. Photographs of the KP samples. (From left to right): intact compact after irradiation; broken compact; pieces of a broken compact; TRISO particles retrieved from a compact.

2.2 THE GAMMA AND NEUTRON DETECTORS

Gamma spectroscopy measurements conducted in this project used three gamma detectors that are available at ORNL: an HPGe detector, a sodium iodide (NaI) detector, and an advanced high-resolution CZT detector, specifically the M400 CZT model. All detectors are depicted in Figure 7, showing that the M400 and NaI are much smaller than the HPGe detector. A comparison of the energy resolutions of the three different types of gamma detectors is presented in Figure 8 [16], showing that the M400 has poorer energy resolution than an HPGe in the energy range of 50–225 keV, but has much better energy resolution than a $LaBr_3$ detector. The NaI, M400, and $LaBr_3$ detectors can all operate under room temperature. Given that the NaI has poorer energy resolution than both the M400 and the $LaBr_3$ detectors, the NaI detector was used only to measure the AGR-2 particles shown in Table 3. The M400 and HPGe detectors were used to measure all the samples shown in Table 1, Table 2, and Table 3.

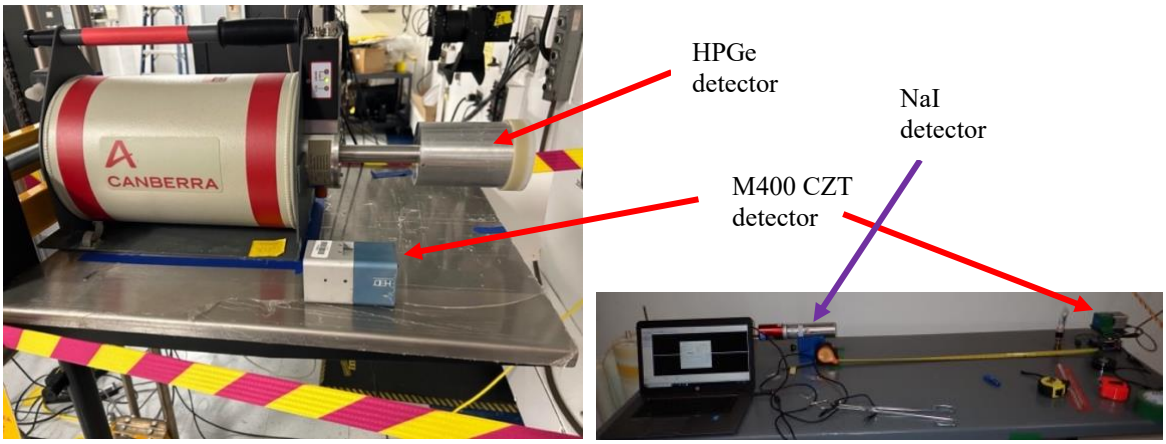

Figure 7. The HPGe and M400 CZT gamma detectors (left) and the NaI detector (right) used in this work.

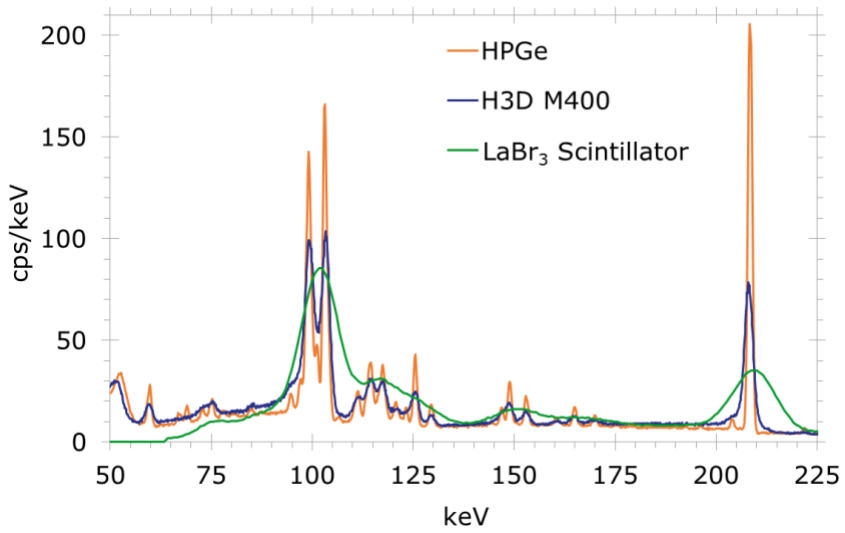

Figure 8. Comparison of energy resolutions of three different gamma spectrometer detectors: HPGe, M400, LaBr3 [16].

The HPGe detector, model BE3825 made by Canberra/Mirion, is a standard broad-energy (for energies ranging from 3 keV to 3 MeV) gamma detector with a 26% relative efficiency. The HPGe detector operates at cryogenic temperatures provided by liquid nitrogen cooling, and it has a full width at half maximum (FWHM) resolution of approximately 0.2% at 662 keV. Data acquisition and signal processing were carried out using the Canberra LYNX digital signal processor with Genie analysis software. Given the HPGe's excellent energy resolutions, the HPGe data are the primary focus of this work.

The M400 CZT detector represents an innovative semiconductor gamma-ray detector technology capable of operating effectively at room temperature, thus eliminating the need for complex cryogenic or mechanical cooling systems. The detector has four crystals, each of which contains 11×11 pixels. This detector achieves an energy resolution of ≤1.1% FWHM at 662 keV. Its ability to function reliably under ambient conditions greatly simplifies operational procedures and enhances its portability. As shown in Figure 9, the M400 CZT detector has recently been authorized by the IAEA as a standard gamma spectroscopy instrument specifically for fresh uranium fuel measurements, thanks to relatively high energy resolution and portability [17]. However, before this work, the suitability and performance of the M400 CZT detector had not been systematically evaluated for the more challenging task of measuring irradiated or spent nuclear fuel. The rare availability of irradiated TRISO fuel samples with varying attributes (e.g., burnup, cooling time) provides a good test bed for this advanced gamma detector.

Figure 9. The M400 CZT gamma detector has been incorporated into an IAEA handheld device (HM-6) and has been authorized for safeguards measurements of fresh uranium materials including UF_6 cylinders [17].

The neutron measurements conducted in this project utilized two neutron detection systems: a custom-built neutron detector specifically designed for this project, and the VPMC detector developed for a prior NA-22 project [8]. The custom-built detector was made with He-3 tubes and materials available at the time at ORNL to meet the measurement timeline, and thus the detector is referred to as the "Makeshift" detector in this project. As shown in Figure 10, the Makeshift detector was made to fit within a 4-in. collimator hole in the hot cell wall to eliminate the need to load the detector into the hot cell, thereby avoiding additional costs and contamination risks. The detector comprises four He-3 tubes (each approximately 1 in. in diameter and 13 in. in length, filled with CO_2 quench gas at 4 atm), embedded within a cylindrical body made of high-density polyethylene (HDPE). This HDPE moderator effectively thermalizes neutrons, enhancing detection efficiency. The HDPE body is wrapped on its sides with a 1-mm-thick cadmium sheet followed by an aluminum sheet. The cadmium sheet was to reduce the thermal neutrons from the background. Initial neutron measurements in September 2023 revealed elevated background neutron counts, which hindered accurate measurements of neutron emissions from the irradiated TRISO samples. To mitigate this issue, two additional 1-inch-thick polyethylene disks and a 1-mm-thick cadmium disk were added to the detector's end facing the hot cell, before subsequent measurements in December 2023, to further reduce the background interference.

Figure 10. (Left) the neutron detector being tested at ORNL's Safeguards Extension Laboratory using a californium neutron source; (right) the two polyethene disks (1 in. thick each) and the cadmium disk (1 mm thick) added to the neutron detector for the December 2023 experiment.

The VPMC, as depicted in Figure 11, is a specialized neutron detection system developed at ORNL, originally designed for nuclear data studies. It comprises 117 He-3 tubes with 7 and 14 atm fill pressure. It offers high detection efficiency and precise measurement capabilities, making it a good candidate to measure individual irradiated TRISO particles. Key features of the VPMC include a neutron detection efficiency of approximately 86%, which significantly improves the accuracy of neutron multiplicity measurements. The system has a die-away time of 19 microseconds, allowing for rapid discrimination between correlated and uncorrelated neutron events. Its lower limit of detection is about 0.07 micrograms of ^{244}Cm over a 3600-second counting period, enabling the detection of minute quantities of fissile material. These attributes make the VPMC potentially useful for measuring small fuel samples. Before this project, the VPMC had not been tested for measuring spent fuel.

Figure 11. The VPMC detector used in this work to measure individual irradiated TRISO particles.

2.3 THE GAMMA MEASUREMENTS PERFORMED

Table 4 provides a comprehensive summary of all gamma-ray measurements conducted, covering efforts performed both at the hot cells and at the SEL. For the KP and AGR samples located within the hot cells of the IFEL, gamma detectors were positioned at varying distances from the outer walls of the cells during the measurements. Conversely, individual AGR-2 and AGR-5 TRISO particles were measured in the SEL, again using both gamma detectors placed at several distinct distances from the samples.

Table 4. The list of conducted gamma measurements.

Measurement month	Samples	Measurement performed
July 2023	The AGR5-RS24 particle	HPGe and M400 measurements at several standoffs (6 to 36 in.) at SEL
September 2023	All AGR samples listed in Table 1	HPGe and M400 measurements of all these samples at various standoffs to maximize the count rates while keeping the deadtime to be less than 60% in the hot cell
December 2023	All the KP samples listed in Table 2 and the two intact AGR compacts listed in Table 1	HPGe and M400 measurements of all these samples at various standoffs to maximize the count rates while keeping the deadtime to be less than 60% in the hot cell
April 2025	All the AGR particles listed in Table 3 and a Cs-137 source standard and an Eu-152 source standard	HPGe, M400, NaI measurements of all these samples at standoffs varying from 6 to 36 in.

The left of Figure 12 shows the experimental setup used for gamma measurement of fuel samples inside a hot cell. As shown, the fuel samples were placed near the mid-height of the collimator slit inside the hot cell, supported by a lab jack. The lab jack itself rested upon a wooden block, which was treated with fire-retardant paint, and then on a polyethylene collar. This setup was improvised to accommodate the limited space in the hot cell and the existing hardware. The right of Figure 12 depicts the arrangement for one of the gamma measurement setups located outside the hot cell. Magenta-colored tape was used to mark a radiation control zone whenever measured radiation levels exceeded the threshold of 2 mRem/h. The radiation zone was needed during the September measurement when either of the two intact AGR compacts was put in place for the gamma measurement; however, such a radiation zone was not needed during any of the December measurements (including the measurements of those AGR compacts), likely owing to the movements of other fuels inside the hot cell. The collimator used in the gamma measurement is shown in Figure 13.

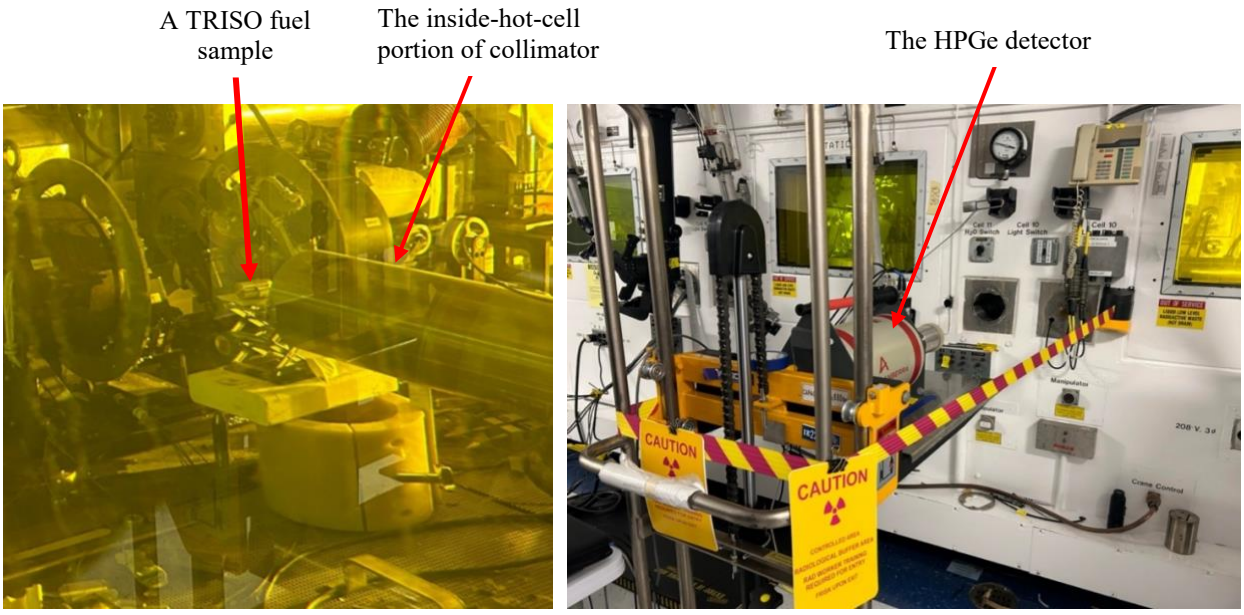

Figure 12. (Left) the setup in the hot cell for the gamma measurements; (right) the setup of an HPGe gamma measurement with the front surface of the detector being a few inches away from the exterior wall of the hot cell and the radiation zone outlined by the magenta tape.

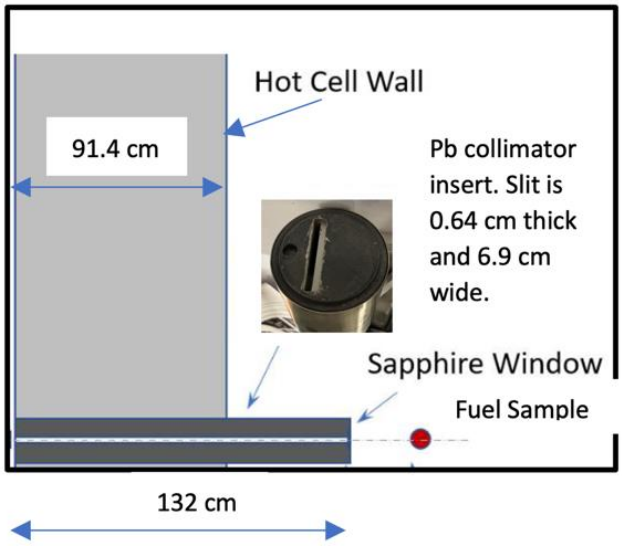

Figure 13. A sketch of the collimator used in the gamma measurement.

Figure 14 and Figure 15 present examples of gamma spectroscopy measurements carried out using the HPGe and M400 CZT detectors, respectively, at two distinct distances between the detector and the samples located in the hot cells. During all gamma measurements, careful adjustments of these distances were performed to maintain detector dead times below 50%, to ensure optimal counting efficiency and accuracy of results. For the gamma measurements, the lead inserts were inserted back into the collimator, and the slit in each insert was lined up to allow the photons from the fuel sample to “shine” through the collimator to the gamma detectors.

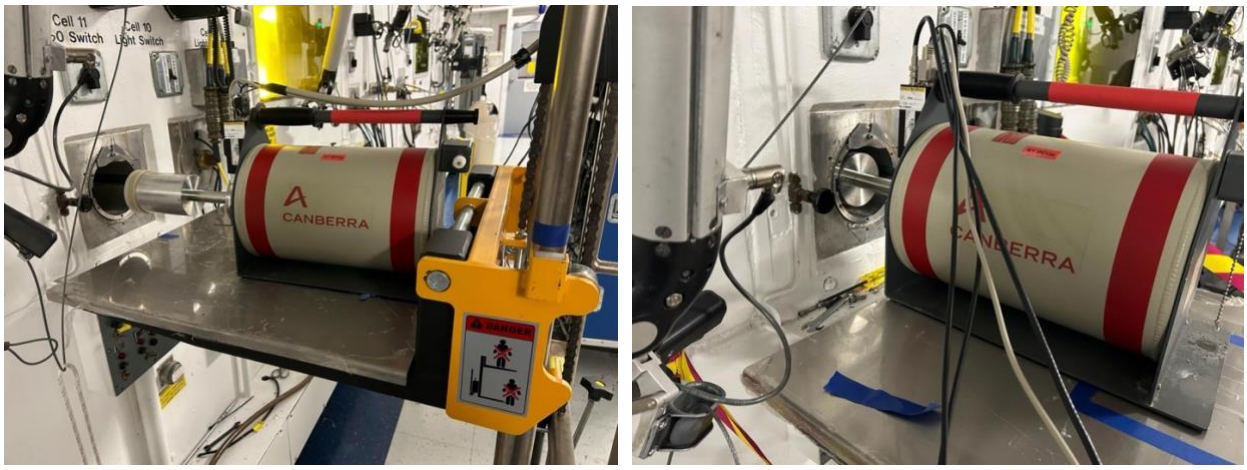

Figure 14. (Left) the setup of an HPGe gamma measurement with the front surface of the detector several inches away from the exterior wall of the hot cell; (right) the setup of an HPGe gamma measurement with the front part of the detector inserted into the port of the collimator.

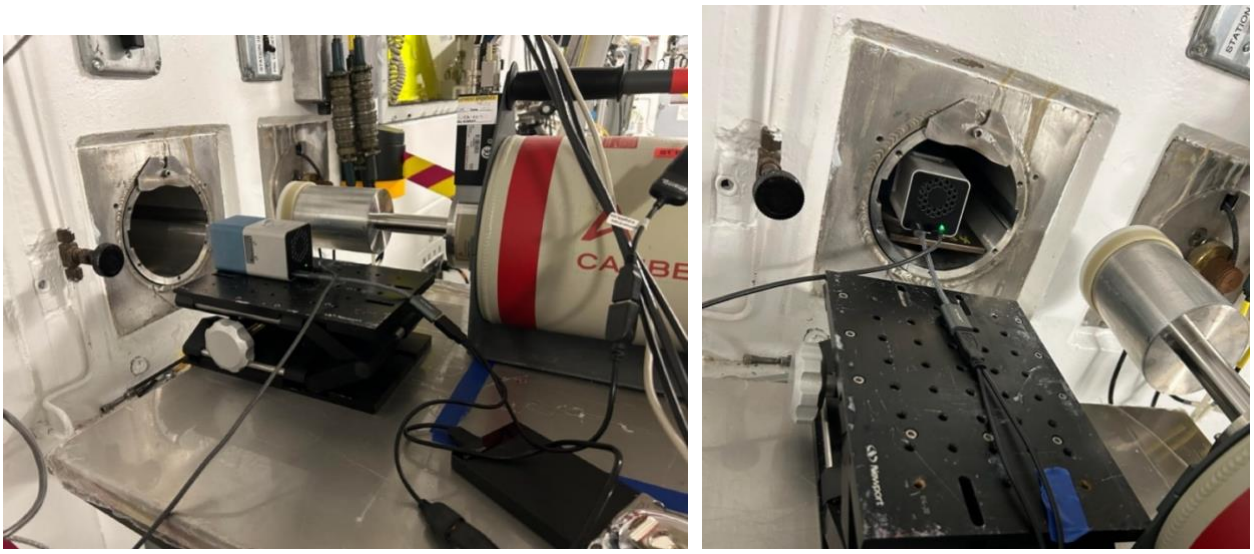

Figure 15. (Left) the setup of an M400 CZT gamma measurement with the front surface of the detector several inches away from the exterior wall of the hot cell; (right) the setup of an M400 CZT gamma measurement with the detector inserted into the port of the collimator.

Figure 16 and Figure 17 illustrate gamma spectroscopy measurements performed with the HPGe and M400 CZT detectors, respectively, on an irradiated TRISO particle at SEL. By leveraging the availability of the TRISO particles at SEL at the time, initial laboratory measurements were conducted on an AGR-5 TRISO particle in July 2023, followed by subsequent measurements on an individual AGR-2 particle in April 2025.

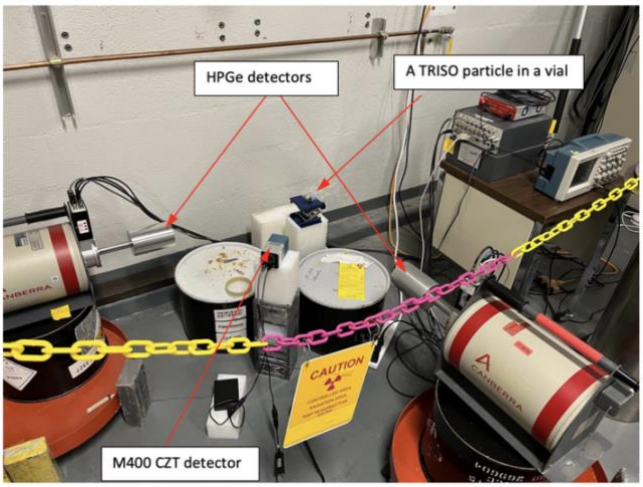

Figure 16. An irradiated AGR-5 TRISO particle was measured using two HPGe detectors and an M400 CZT detector at ORNL's SEL.

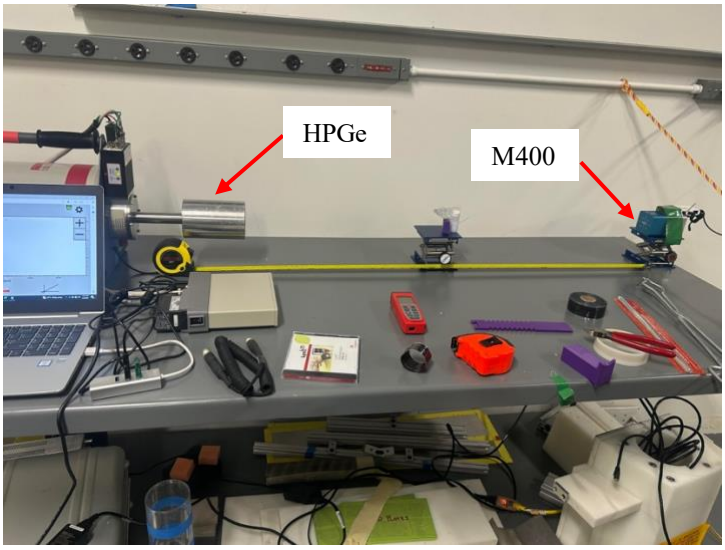

Figure 17. An irradiated AGR-2 TRISO particle was measured using an HPGe detector and an M400 CZT detector at ORNL's SEL.

2.4 THE NEUTRON MEASUREMENTS PERFORMED

Neutron measurements using the Makeshift neutron detector were conducted primarily at SEL and at the IFEL hot cell. Initial testing of the neutron detection systems was performed at SEL during August and September 2023 using a ^{252}Cf neutron source to verify detector performance. Following successful preliminary testing, subsequent measurements were carried out in the IFEL hot cell starting in September 2023, initially focusing on the three most radioactive AGR samples. In December 2023, the KP samples were measured in addition to the previously measured AGR samples.

The Cf-252 neutron source employed for the initial testing of the Makeshift neutron detector was designated as Cf6081, with a neutron emission rate of approximately 1.05×10^5 neutrons per second. Detector performance evaluation was conducted by measuring neutron response across varying high-voltage biases, confirming operational consistency and expected behavior, as illustrated in Figure 18. Based on these results, a bias voltage of 1700 V was applied when the ^{252}Cf source was positioned at 1 in.

from the detector's edge (slightly closer compared with the position used in the tests to generate the results shown in Figure 18) for measurement, the neutron singles count rate was measured at 1042.5 ± 0.9 cps, and the doubles rate was 23.3 ± 0.4 cps for the ^{252}Cf source. The Makeshift detector measured low background counts at SEL, with a singles count rate of 0.59 ± 0.004 cps, with no double counts detected.

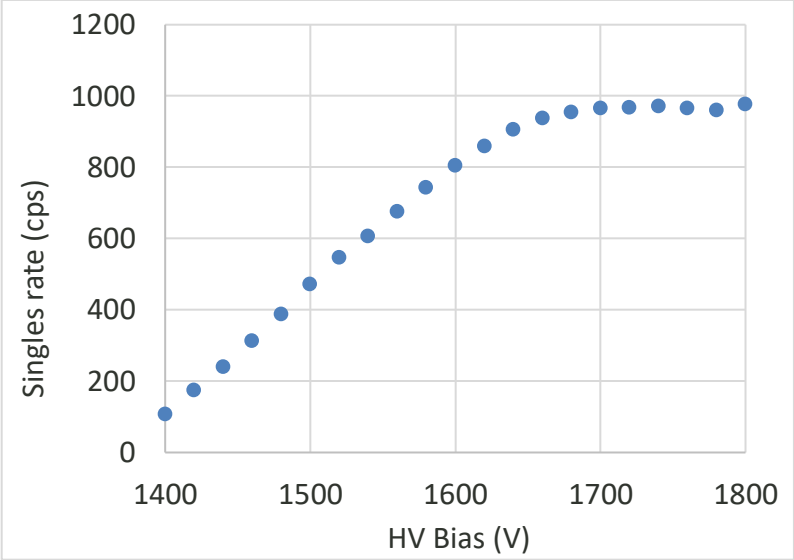

Figure 18. Singles rate as a function of high-voltage bias of makeshift neutron detector with Cf-252 source.

During the hot cell measurement, the neutron detector was inserted inside the collimator (with all lead inserts removed except for the very last one), and the irradiated fuel samples were carefully placed in an aluminum tray atop a polyethylene sleeve surrounding the collimator to optimize neutron moderation and detector response, as shown in Figure 19. Neutron moderation is needed for this kind of measurement because the neutrons emitted by the fuel are mostly fast neutrons, and the He-3 tubes in the Makeshift detector are mostly sensitive to thermal neutrons.

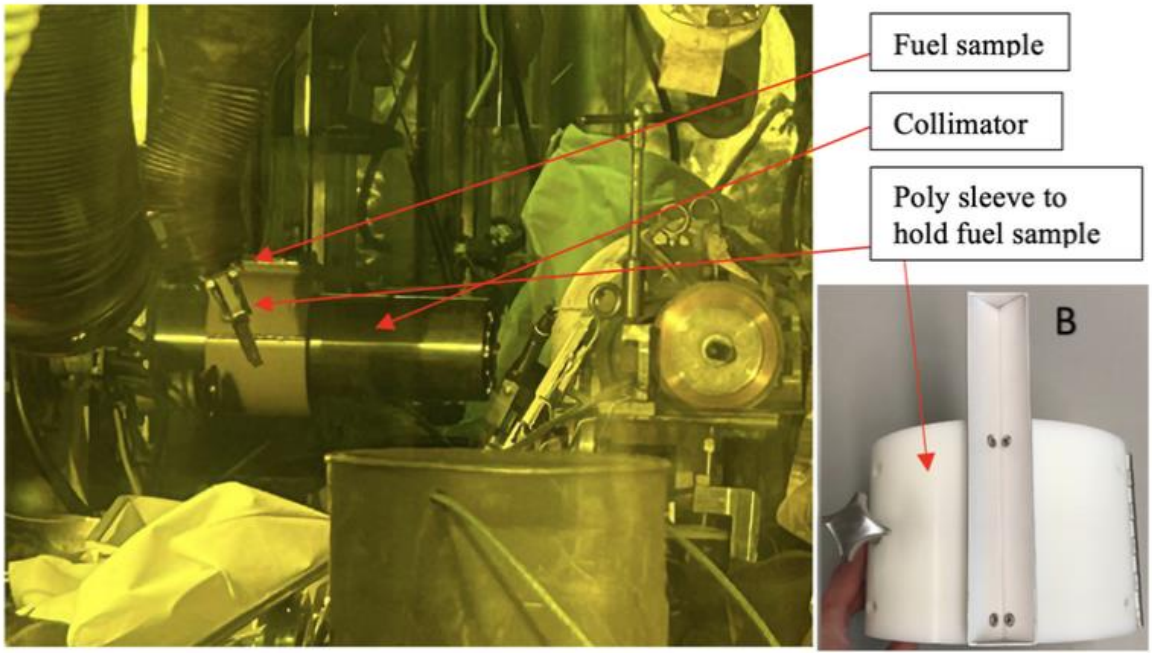

Figure 19. Makeshift neutron detector during hot cell measurement

Initially, measurements encountered significant challenges: background neutron count rates, recorded without the TRISO fuel samples in place, were found to be high. They were sometimes even higher than the count rates with samples in place, which led to a net negative singles rate of -7.8 ± 0.2 cps for the AGR-5 compact. It was determined that the high background counts were from the legacy nuclear materials accumulated in the hot cell over decades, including the pressurized water reactor (PWR) spent fuel segments illustrated in Figure 20.

Figure 20. Some of the PWR spent fuel segments stored in the same hot cell where these neutron and gamma measurements were performed.

To overcome this high background issue, an iterative approach was implemented involving several incremental adjustments aimed at reducing background interference. Three major modifications were sequentially performed to reduce the neutron background. The most significant improvement was

achieved by adding the polyethylene and cadmium disks, shown in Figure 10 (right), to the detector's front end. These disks significantly suppressed unwanted background neutrons through a combination of neutron moderation by polyethylene and neutron absorption by cadmium, drastically reducing background count rates. Further incremental improvements were accomplished by physically relocating legacy commercial nuclear fuel rodlets to positions further away from the measurement region. Additionally, placing the remaining AGR samples behind a polyethylene block provided additional reductions. Figure 21 illustrates the progressive reductions in neutron background count rates achieved after each step. Figure 22 and Figure 23 further highlight these improvements by comparing the neutron count rates with their respective background counts for the measurements of the AGR-5-223 compact. The averages of the background measurement and the measurement of the AGR-5-223 compact are indicated by dashed lines in both figures. Following the implementation of all these background reduction measures, significant reductions in background count rates can be seen in Figure 23 compared with Figure 22, for example, the average background count rates were reduced from 2239 (in Figure 22) to 519 (in Figure 23).

This significant reduction enabled the acquisition of positive net neutron count rates, which is indicated by the higher average count rates in the AGR-5-223 compact measurement than in the background measurement shown in Figure 23. After mitigation, the AGR-5-223 compact yielded a net singles neutron count rate of 2.3 ± 0.5 cps. Similarly, the KP-125 compact produced a net singles count rate of 3.1 ± 0.5 cps. Despite achieving these measurement improvements, the experimental schedule constraints and limited available measurement time prevented further characterization of additional samples within this effort. Additionally, throughout all conducted neutron measurements, net neutron doubles count rates remained effectively at zero owing to the small amounts of nuclear materials in these TRISO samples.

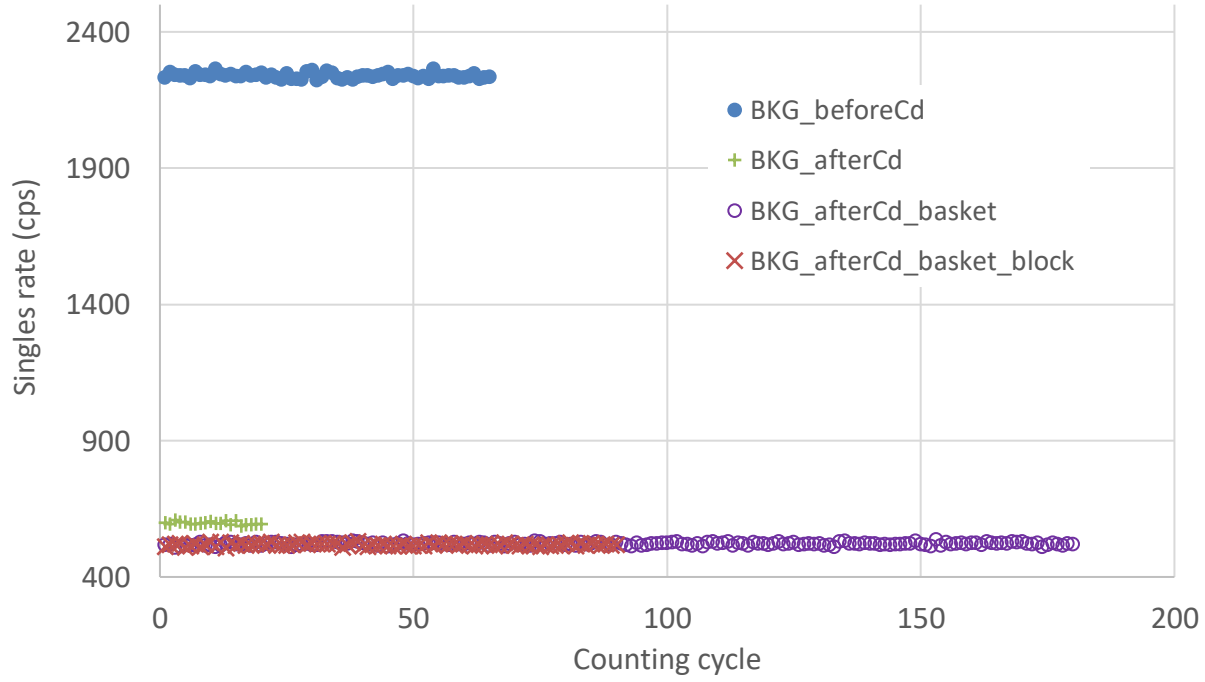

Figure 21. The neutron background ("BKG") count rates after four different steps taken to reduce them.

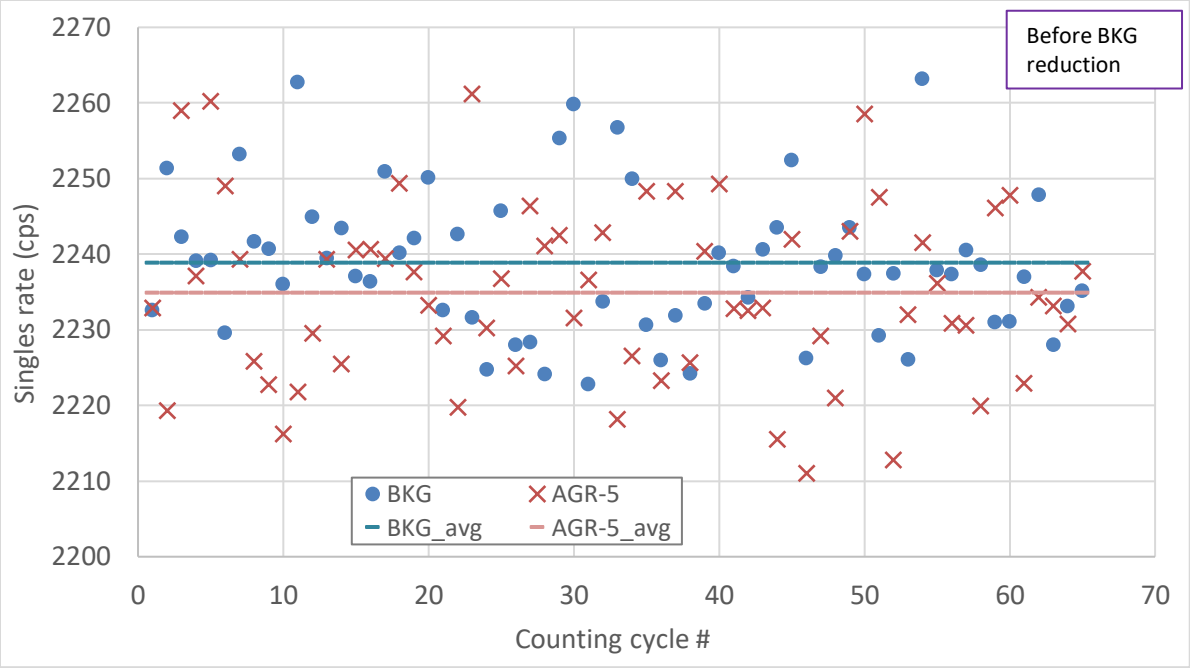

Figure 22. The neutron count rates during the background measurements and the measurement of the AGR-5-223 compact before steps taken to reduce the background.

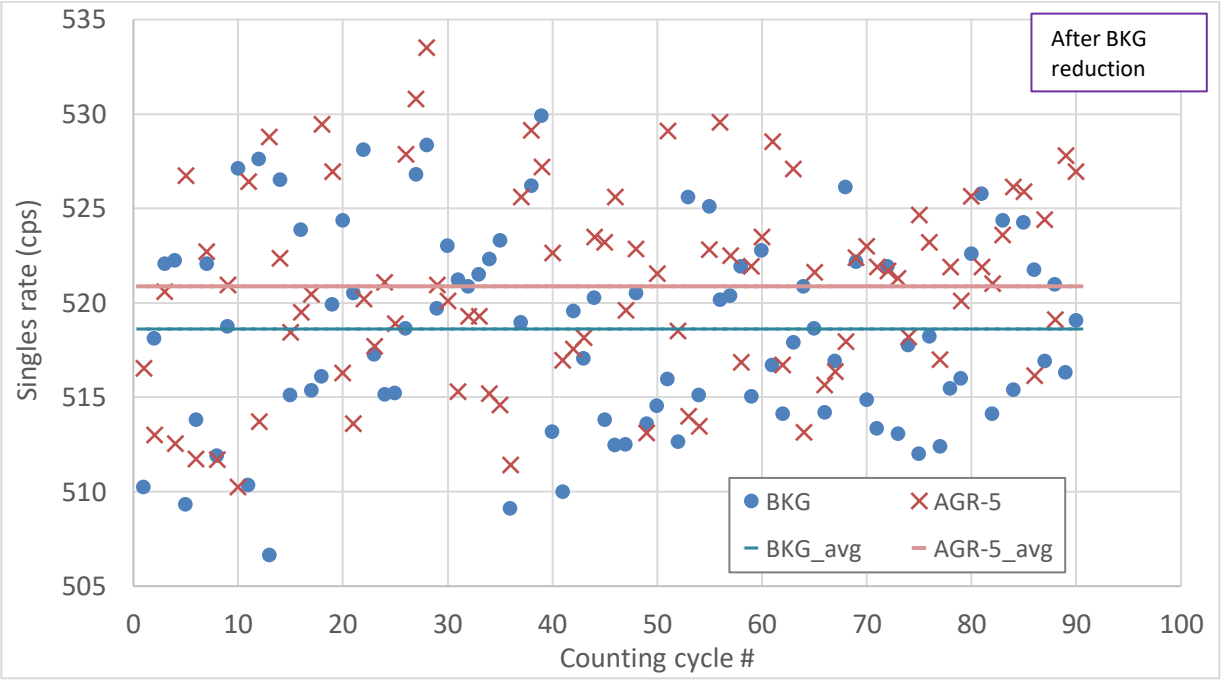

Figure 23. The neutron count rates during the background measurements and the measurement of the AGR-5-223 compact after steps taken to reduce the background.

High-voltage plateau tests were conducted to assess the neutron detector's operational performance under the high neutron and gamma-ray backgrounds in the hot cell. These measurements, as shown in Figure 24, demonstrated the significant impact of elevated gamma-ray dose rates originating predominantly from adjacent spent commercial nuclear fuel rods and rodlets. Because of spatial and operational constraints

within the hot-cell environment, it was not feasible to incorporate additional gamma-ray shielding directly around the neutron detector. Consequently, gamma dose rates at the He-3 detector tube location were estimated to be approximately 100 R/h, comparable to the radiation environment typically encountered when measuring spent fuel pebbles. To mitigate the adverse effects of such intense gamma radiation on detector operation, specifically gamma-induced noise and elevated baseline count rates, the detector's operating voltage was deliberately reduced from its standard high-voltage setting of 1700 V to 1600 V for these hot cell measurements. Although this approach effectively reduced gamma sensitivity, it resulted in a trade-off, lowering neutron detection efficiency by approximately 25%.

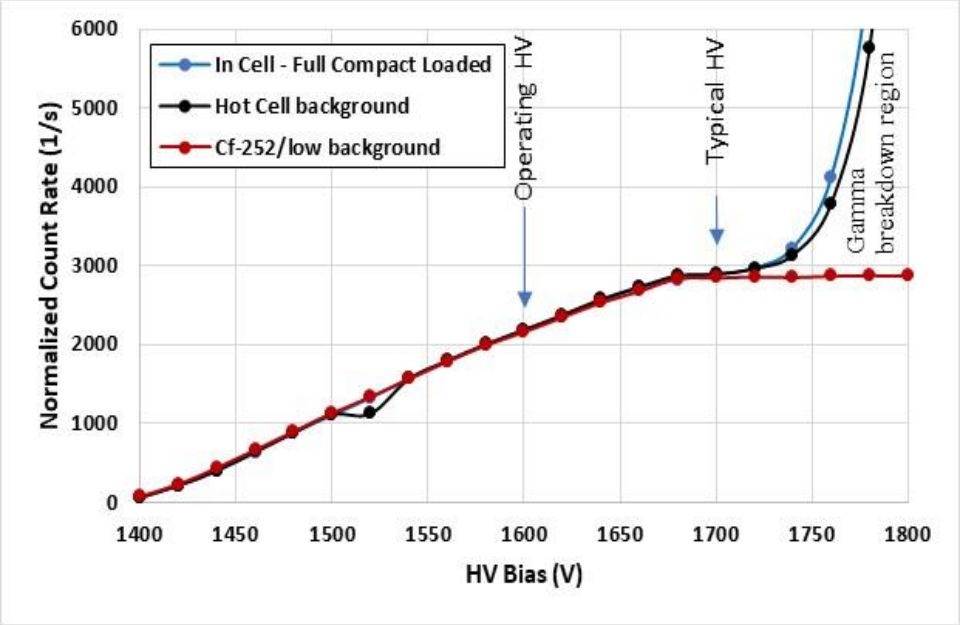

Figure 24. Measured high-voltage plateaus illustrating the impact of the high neutron and gamma-ray background on the measurements in the hot cell.

3. ANALYSIS OF THE GAMMA MEASUREMENTS

3.1 QUALITATIVE ANALYSIS

The shape, magnitude, and peaks of a gamma spectrum are affected by parameters such as the detector type, standoff (i.e., distance between the source and the front surface of the detector), and source attributes. As for the irradiated TRISO samples, the burnup and cooling time (i.e., the time since the end of the irradiation in the reactor) are the two most important attributes. A series of spectrum comparisons are included in this section to provide a quantitative assessment on how each of these factors affected the measured spectra, especially in the energy range of 600 to 800 keV, focused on the two major ^{134}Cs peaks (604 and 796 keV) and the main ^{137}Cs peak (662 keV).

Figure 25 compares the gamma spectra among the three different gamma detectors described in the previous section. The measured sample was the AGR-2-XR143 particle, and the standoff was 6 in. As shown, the HPGe detector shows much superior energy resolution to both the M400 and NaI detectors—like what is shown in Figure 8 but in a much wider energy range. The FWHMs of the HPGe, M400, and NaI detectors are 1.3, 4.3, and 50.7 keV at the 662 keV peak, respectively, representing relative energy resolutions of 0.20, 0.65, and 7.66%. More peaks can be observed in the HPGe spectrum than in the M400 spectrum owing to the HPGe's higher energy resolution. For the three major Cs-134 and Cs-137 peaks, M400 was able to measure both the 604 and 662 keV peaks like the HPGe, but M400 could not resolve the two closely spaced peaks at 796 and 804 keV. Compared with the HPGe detector, the detection efficiency of the M400 significantly decreased after 662 keV. The NaI detector could not resolve the 605, 662, and 721 keV peaks. As shown in these results, the M400 (an advanced room-temperature detector) has significant performance improvements over the NaI detector, which is one of the conventional room-temperature detectors.

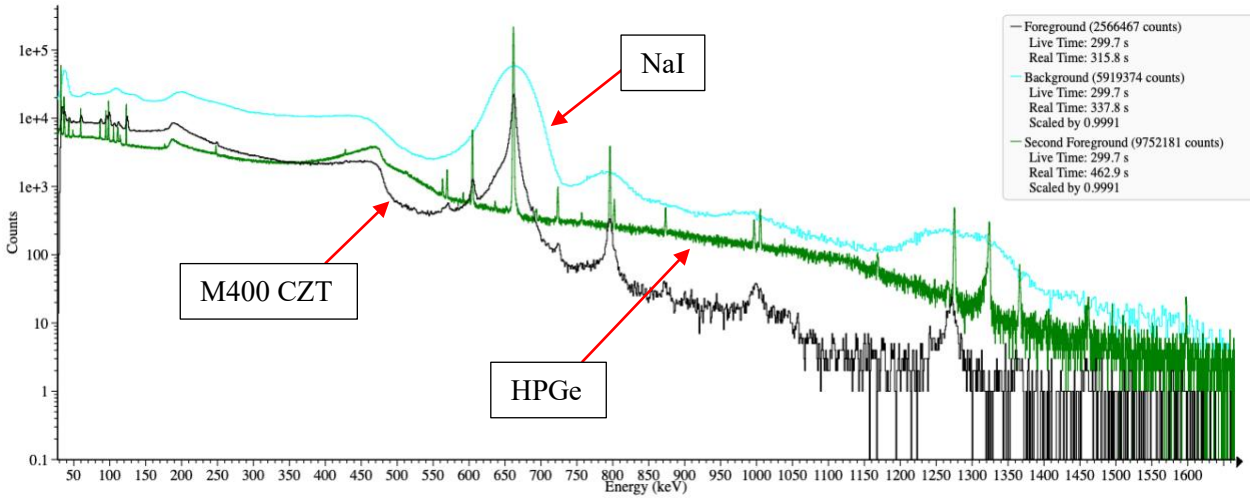

Figure 25. Comparison of the measured gamma spectra among three different gamma detectors. The sample was the AGR-2-XR143 particle, and the standoff was 6 in.

Figure 26 compares the gamma spectra measured from three different samples by the HPGe detector: the AGR-2-XR143 particle (with a burnup of 116 GWd/MTU), the AGR-2-XR136 particle (with a burnup of 72 GWd/MTU), and the ^{137}Cs source standard. As expected, more peaks were measured in the two TRISO particles than in the ^{137}Cs source, whose minor peaks are likely from the impurities contained in the source. Similar spectra were measured from the two AGR-2 particles, except that higher peaks and continuum were measured from the XR143 particle than from the XR136 particle because of the former's

higher burnup value. Figure 27 makes the same comparison as in Figure 26, but for the M400 detector, and similar observations can be made.

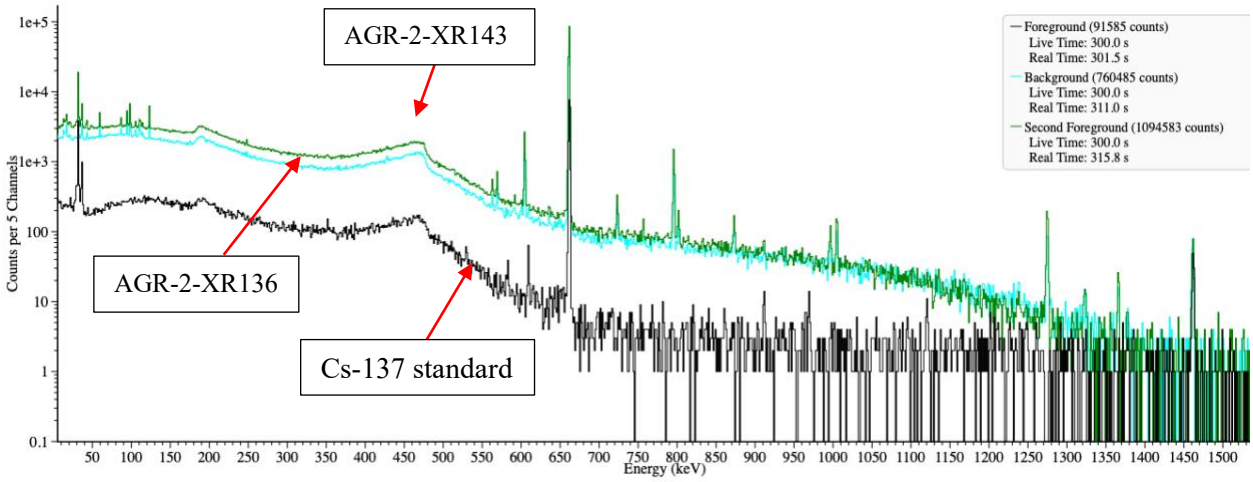

Figure 26. Comparison of the measured HPGe gamma spectra among three different samples. The standoff was 21 in.

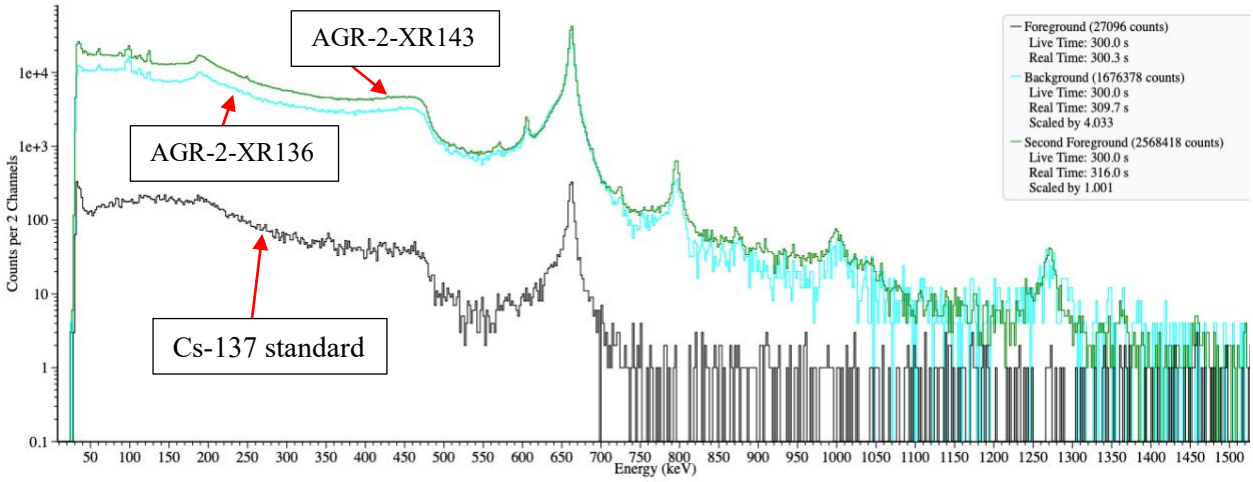

Figure 27. Comparison of the measured M400 gamma spectra among three different samples. The standoff was 21 inches.

Figure 28 presents a comparison of the measured HPGe gamma spectra for the AGR2 XR143 particle at two distinct standoff distances: 6 in. and 21 in., with the spectrum for the latter depicted in blue. The figure on the right focuses on the three primary peaks attributed to ^{134}Cs and ^{137}Cs, with the respective peak energies, half-lives, and yields annotated within the boxes. As anticipated, the spectral shapes at both standoff distances are similar. However, the overall count rates, including those of the three Cs peaks, at the 21-in. standoff are approximately an order of magnitude lower than those observed at the 6-in. standoff.

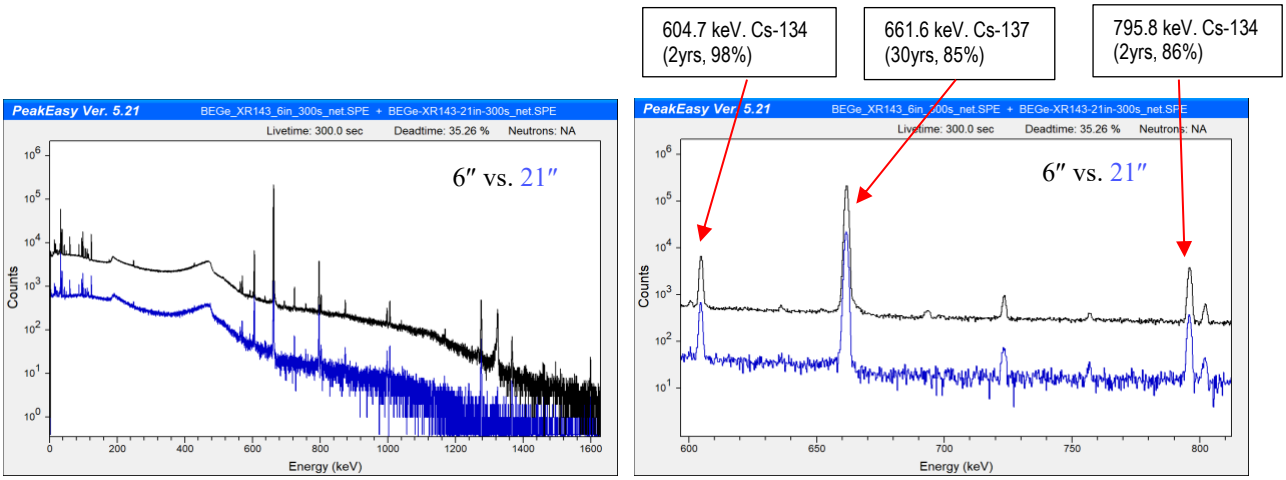

Figure 28. (Left) Comparison of the measured HPGe gamma spectra of the AGR-2 XR143 particle taken at two different standoffs: 6-in. vs. 21-in. (blue); (right) zoomed in the [600, 800] keV range.

Figure 29 compares the measured HPGe gamma spectra between the AGR5-RS24 particle and the AGR2-XR143 particle. The standoff of both measurements was 21 in. The burnups of these two particles are similar (135 vs. 116 GWd/MTU), but their cooling times are very different: 3 years for the AGR-5 particle and 12 years for the AGR-2 particle. The spectrum corresponding to the 12-year cooling time is shown in blue. As expected, fewer peaks are observed in the case with the longer cooling time. The overall count rates, including those of the three Cs peaks, at the shorter (3-year) cooling time, are significantly higher than those observed at the longer (12-year) cooling time.

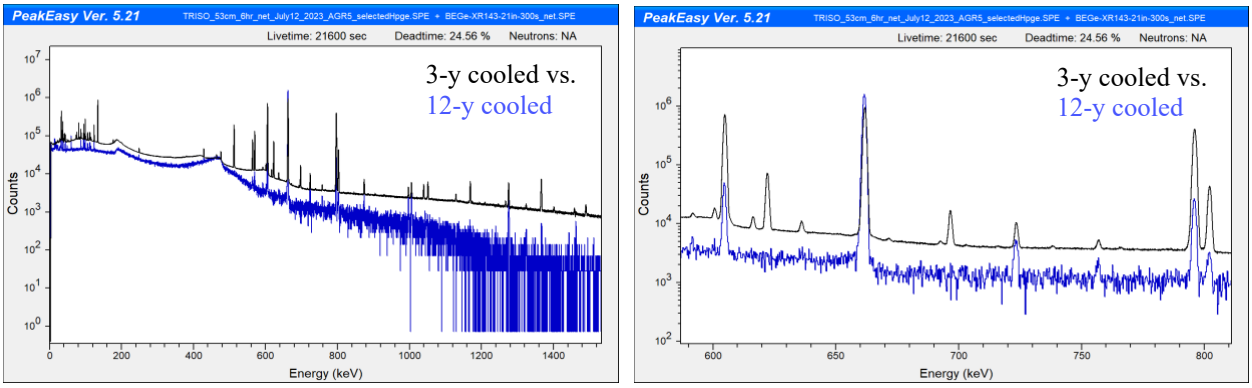

Figure 29. (Left) Comparison of the measured HPGe gamma spectra of the AGR5 and AGR2 particles taken at two different cooling times: 3-year (in black) and 12-year (in blue); (right) zoomed in the [600, 800] keV range.

Figure 30 compares the measured HPGe gamma spectra of the AGR2-XR136 and AGR2-XR143 particles, both acquired at a 6-in. standoff. The spectrum for AGR2-XR136 is shown in blue. As expected, the spectral shapes for both particles are similar. However, the overall count rates, including those of the three Cs peaks of the lower-burnup case, are significantly lower than those of the higher-burnup case.

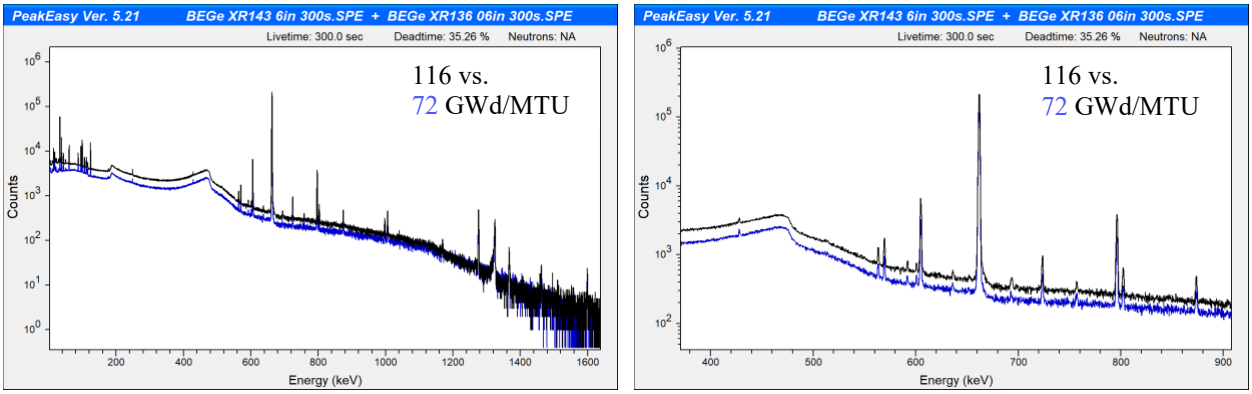

Figure 30. (Left) Comparison of the measured HPGe gamma spectra: the AGR2-XR143 (115.7 GWd/MTU) particle vs. the AGR2-XR136 (71.6 GWd/MTU) particle (blue); (right) zoomed in the [400, 900] keV range.

Figure 31 compares the measured HPGe gamma spectra of the AGR2-211 compact and the AGR2-XR143 particle, with the spectrum for AGR2-XR143 shown in blue. The spectra for both cases exhibit similar shapes. However, the overall count rates, including those of the three Cs peaks, for the AGR2-211 compact are approximately an order of magnitude lower than those for the AGR2-XR143 particle. The burnups of the compact and of the particles are similar (120 vs. 116 GWd/MTU), but the AGR-2 compact contains 3176 particles. The difference in these two spectra can be attributed to two factors: the compact was measured through a collimator that allows only a fraction of gamma rays to reach the detector and has a ~4× longer standoff than the particle.

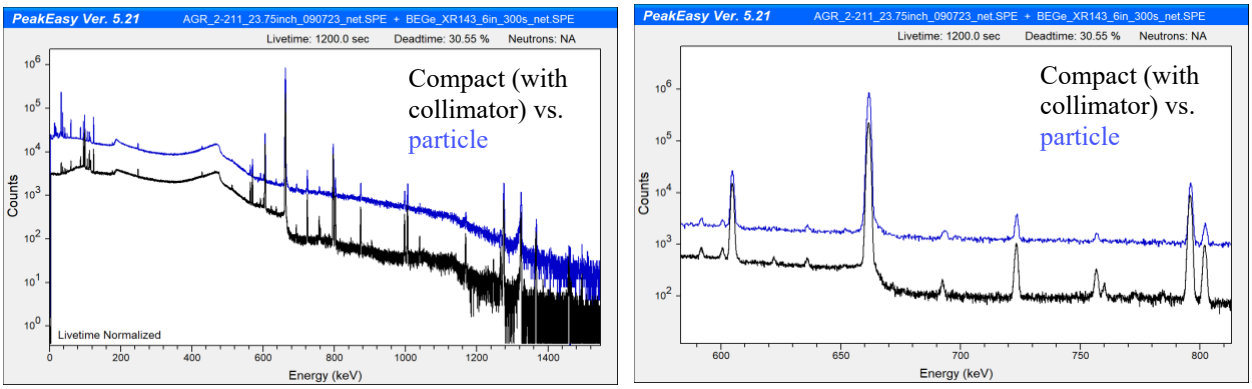

Figure 31. (Left) Comparison of the measured HPGe gamma spectra: the AGR2-211 compact vs. the AGR2-XR143 particle (blue); (right) zoomed in the [600, 800] keV range. Note the compact was measured through a collimator at ~4× longer standoff than that of the particle.

Figure 32 compares the measured gamma spectra of the AGR-5-RS24 particle acquired using both the HPGe detector and the M400 detector, with the M400 spectrum shown in blue. The standoff for both was 21 in. Similar to what is shown in Figure 25, higher energy resolution and more gamma peaks are observed in the HPGe spectrum than in the M400 spectra, although the M400 was able to detect and resolve the 604 and 662 keV peaks. An approximately 10× lower continuum can be observed in the M400 after the 662 keV peak, indicating a steeper detection efficiency decrease at higher energies in the M400 detector than in the HPGe.

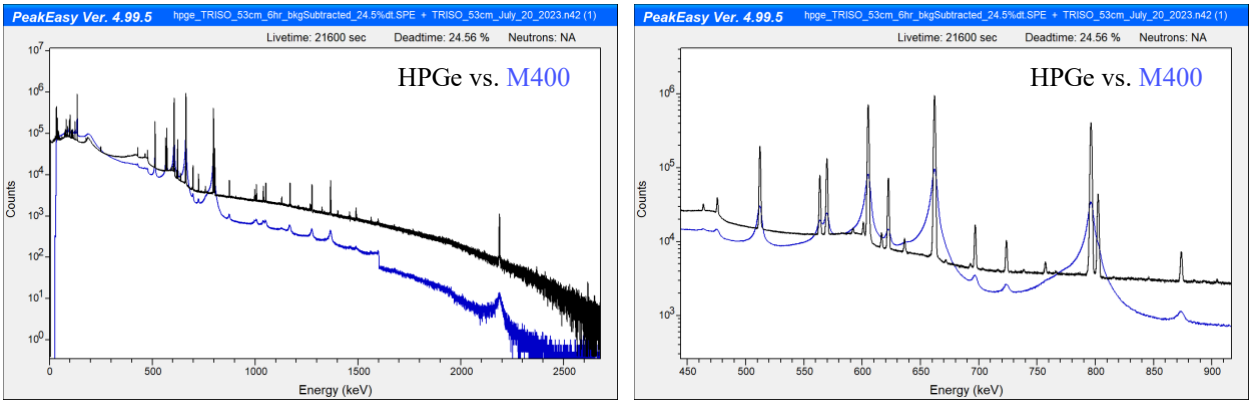

Figure 32. (Left) Comparison of the measured gamma spectra of the AGR-5-RS24 particle: HPGe vs. M400 (blue); (right) zoomed in the [450, 900] keV range.

Figure 33 compares the measured HPGe gamma spectra of the AGR5-223 and AGR2-211 compacts, with the spectrum of the AGR-2 compact shown in blue. The same standoff was used in both measurements. The burnups of these two compacts are similar (138 vs. 120 GWd/MTU, see Table 1), but the cooling times are very different (3 years vs. 10 years). As expected, higher count rates (including those of the three Cs peaks) and more peaks can be observed in the compact with a shorter cooling time. Unlike the 604 and 796 keV peaks, the 662 keV peak for the AGR5-223 is only slightly higher than that of the AGR2-211 compact with a longer cooling time due to Cs-137's much longer half-life compared with ^{134}Cs (30 years vs. 2 years).

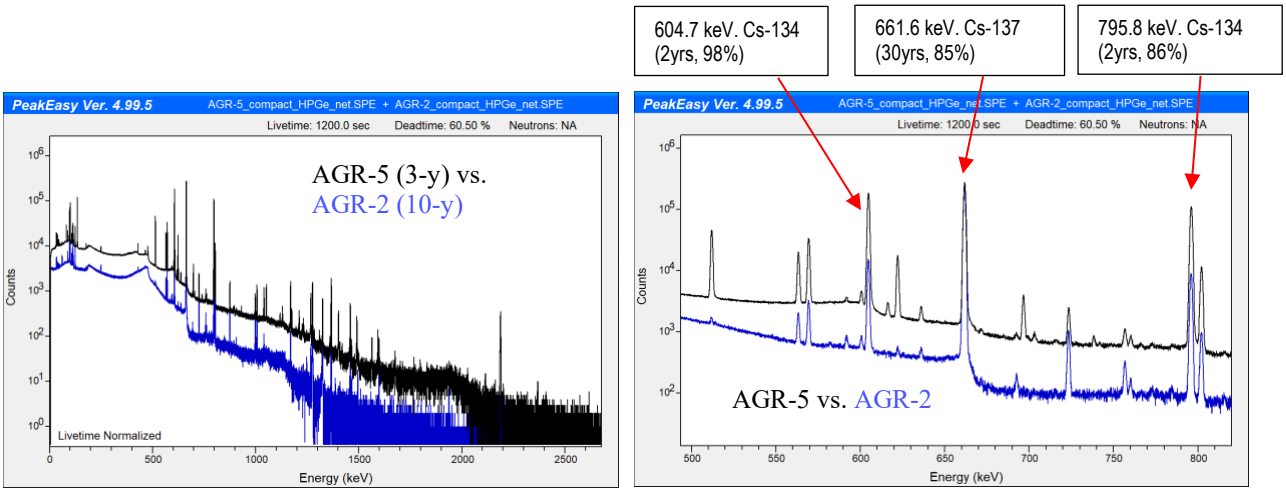

Figure 33. (Left) Comparison of the measured HPGe gamma spectra of the two AGR compacts: AGR5 vs. AGR2 (blue); (right) zoomed in the [500, 800] keV range.

Figure 34 shows a similar comparison of gamma spectra of the AGR5-223 and AGR2-211 compacts as in Figure 33, but this is for the M400 detector. Similar observations can be made in this figure: that the compact with a shorter cooling time has higher count rates and more peaks than the compact with a longer cooling time.

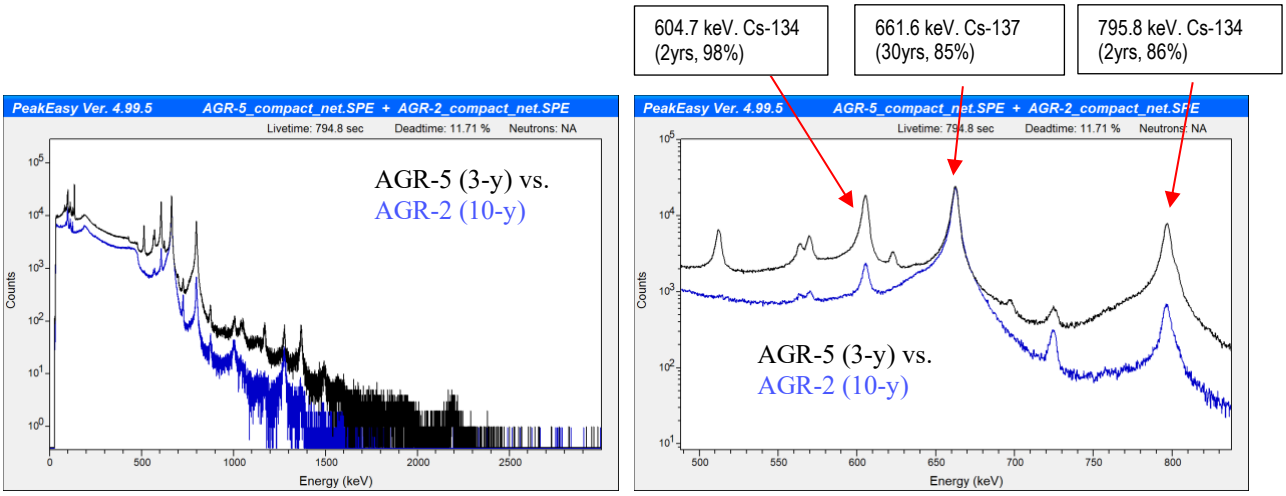

Figure 34. (Left) Comparison of the measured M400 gamma spectra of the two AGR compacts: AGR5 vs. AGR2 (blue); (right) zoomed in the [500, 900] keV range.

Figure 35 compares the measured HPGe gamma spectra of the AGR2-211 and KP-125 compacts, with the spectrum of the KP-125 compact shown in blue. The same standoff was used in both measurements. The burnups of these two compacts were similar (120 vs. 114 GWd/MTU), but the cooling times were very different (3 years vs. 10 years). The AGR-2 compact contained ~176× more particles than the KP-125 compact. The higher number explains the much higher count rates observed in the AGR-2 compact, although the count rates are not proportional to the number of TRISO particles between the two compacts because the fraction of particles directly aligned with the slit in the collimator (see Figure 13) also affects the count rates. Given that the KP-125 compact had a much shorter cooling time than the AGR-2 compact, and ^{134}Cs has a much shorter half-life than ^{137}Cs, stronger ^{134}Cs peaks (e.g., 604 and 796 keV), relative to their respective 662 keV peaks, can be observed in the KP-125 compact than in the AGR-2 compact. Several major peaks are absent from the AGR2-211 spectrum owing to its additional decay time. Notably, these include the 133.51 keV peak from ^{144}Ce, the 621.7 keV peak from ^{106}Ru, the 696.5 keV peak from 144Pr/^{144}Ce, the 756.8 keV peak from ^{95}Zr, and the 765.8 keV peak from ^{95}Nb.

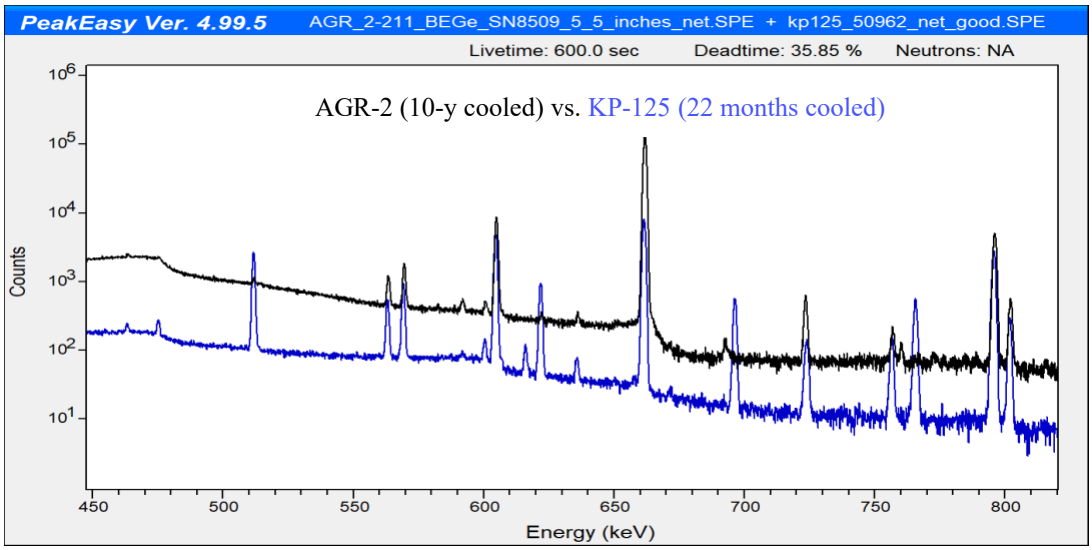

Figure 35. Comparison of the measured HPGe gamma spectra of the two compacts: the AGR2-211 compact vs. the KP-125 compact (blue).

3.2 QUANTITATIVE ANALYSIS

Following the qualitative analysis in the previous subsection, the quantitative analysis of the measured gamma spectra is presented in this subsection. Figure 36 shows the HPGe-measured 662 keV peak area rate (counts per second) of the AGR-5-RS24 particle vs. $1/R^2$, with "R" meaning the standoff in the AGR-5-RS24 particle measurements. As shown, the data points generally follow the linear trend line as expected. The deviations from the trend line can be attributed to the scattering of the gamma rays in the measurement environment.

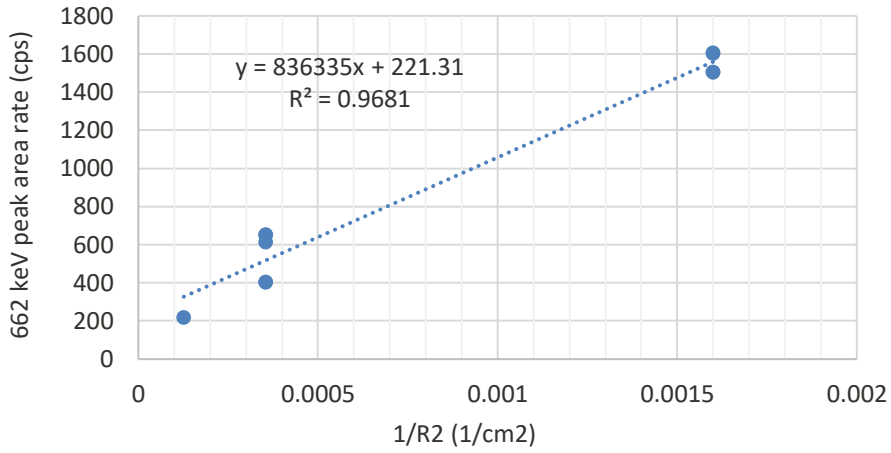

Figure 36. The 662 keV peak area rate vs. $1/R^2$, with "R" meaning the standoff in the AGR-5 particle measurements.

Figure 37 shows the HPGe peak area rates of the 604, 662, and 796 keV peaks vs. the samples' burnup values among all samples measured in the hot cell. The differences in cooling times among all samples are accounted for, so the peak area rates of these three peaks are compared on the same cooling-time basis. The peak area rates are expected to trend positively with burnups, but they also depend on the alignment between the slit and the samples inside the containers. It is impossible to determine what fractions of the gamma rays emitted by the samples traveled through the slit owing to the following factors: (1) the volumes of the samples' containers were significantly larger than the samples' own volumes; (2) the vast majority of the samples were loose particles; (3) the slit was much smaller than the samples' outer surfaces. Although the peak area rates generally trend higher with burnups, large scattering can be seen owing to differences in the number of particles contained in the samples and the standoffs in the measurements. The peak area rates of the 662 keV peak are much higher than those of the two ^{134}Cs peaks in the corresponding cases, which can be attributed to the higher fission yield and longer half-life of ^{137}Cs compared with ^{134}Cs. The peak area rates of the 604 keV peak are slightly higher than those of the 796 keV peak owing to the higher branching ratio and higher detection efficiency of the 604 keV.

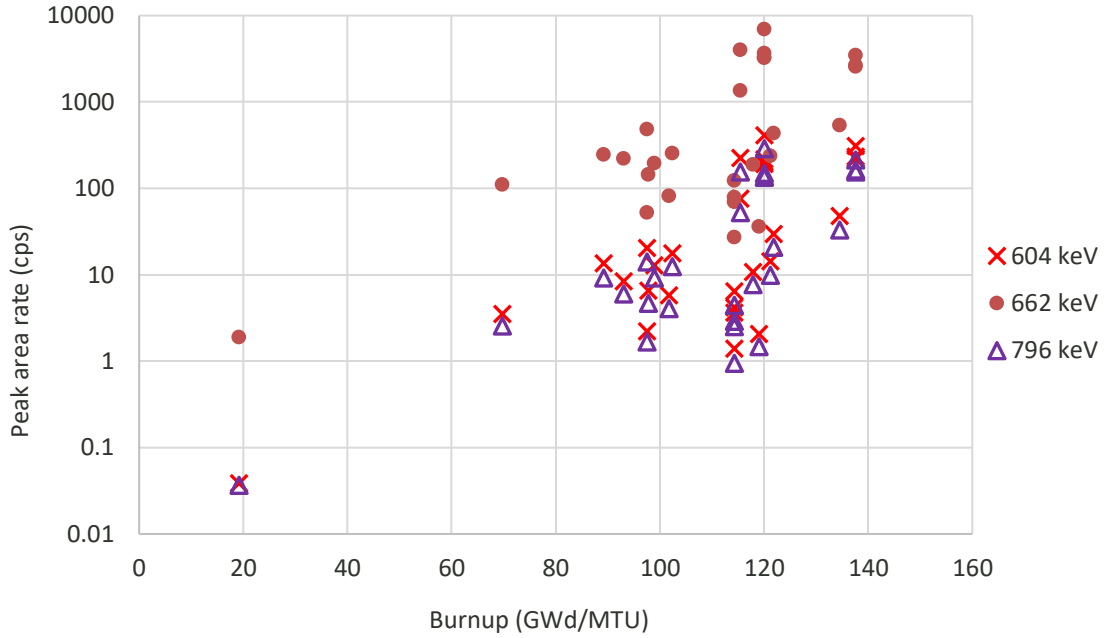

Figure 37. The peak area rates of the 604, 662, and 796 keV gamma lines vs. the samples' burnup values among all samples measured in the hot cell. The differences in cooling times among all samples are accounted for.

Figure 38 shows similar 604 and 662 keV peak results to Figure 37 but on a per-particle basis. The differences in cooling times among all samples are accounted for, so the peak area rates of these three peaks are compared on the same cooling-time basis. There is a general positive trend between the peak area rates with the samples' burnup values, but large scatters still exist, as is expected because of the aforementioned alignment issue between the slit and the samples.

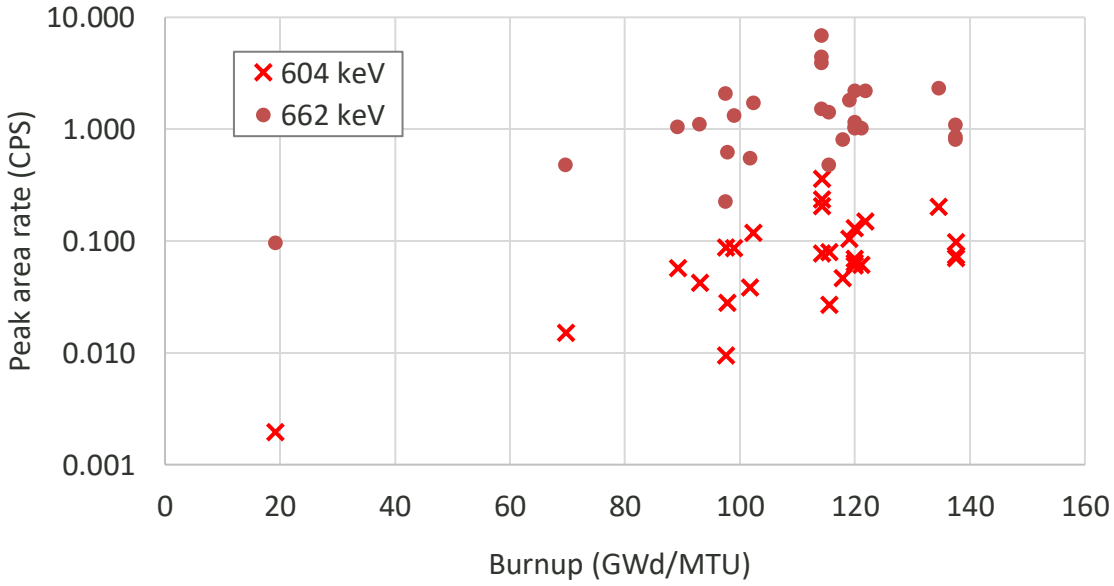

Figure 38. The HPGe peak area rates (per unit particle) of the 604, and 662 keV gamma lines vs. the samples' estimated burnups.

The 604/662 peak area ratios were also often used to infer the spent fuel's burnup. Compared with using absolute peak areas that can be affected by multiple factors (e.g., uncertainties in measurement positioning, source distributions and intensities), the peak ratio benefits from the cancellation effect of the uncertainties; for example, uncertainties in the positions or source intensity will affect both the 604 and 662 keV peak areas in a similar way and thus would have smaller effects on the 604/662 peak ratio. The 604 keV peak of ^{134}Cs is preferred over the other ^{134}Cs peak at 796 keV because the branching ratio and detection efficiency of the 604 keV peak are higher than those of the 796 keV peak. Figure 39 shows the 604/662 peak area ratio vs. the burnup values of the five individual AGR-2 TRISO particles measured at the SEL. In general, positive trends with burnups can be seen for both the 6-in. and 21-in. standoff measurements. Scatters exist around the trend line, which can be attributed to particle positioning uncertainties and gamma-ray scattering in the environment.

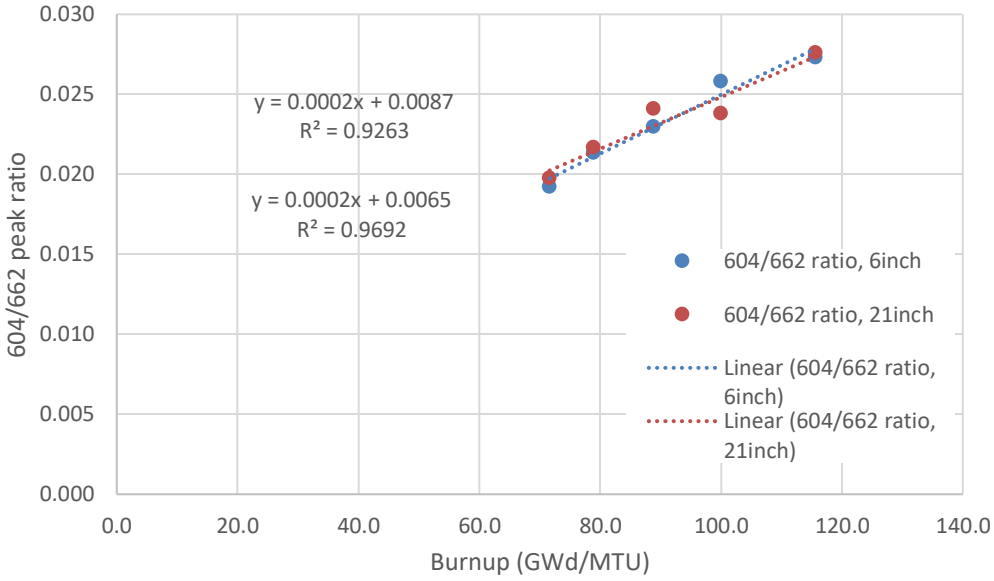

Figure 39. The 604/662 peak area ratios of the 5 AGR-2 particles vs. the samples' estimated burnups.

Figure 40 shows the 604/662 peak area ratios vs. the samples' burnup values among all TRISO samples measured in the hot cell and the AGR-5-RS24 particle. The differences in cooling times among all samples were accounted for, so the peak ratios are compared on the same cooling-time basis. The trendline is generated by fitting a fourth order polynomial function to the data, as depicted in the figure, where "y(x)" is the 604/662 peak area ratio and "x" is the burnup. All data points except for four generally follow the trendline with a standard deviation of 4.7%. Three of those four outlier data points had 9.6% initial enrichments, which are significantly different from the remainder's 14% and 15.5% enrichments. The accumulation of ^{134}Cs was known to be dependent on both the fuel burnup and the neutron spectra when the fuel was irradiated [18], which in turn is sensitive to the fuel's enrichment. The fourth outlier data point was from the AGR5-159A sample, which is a subject of further investigation.

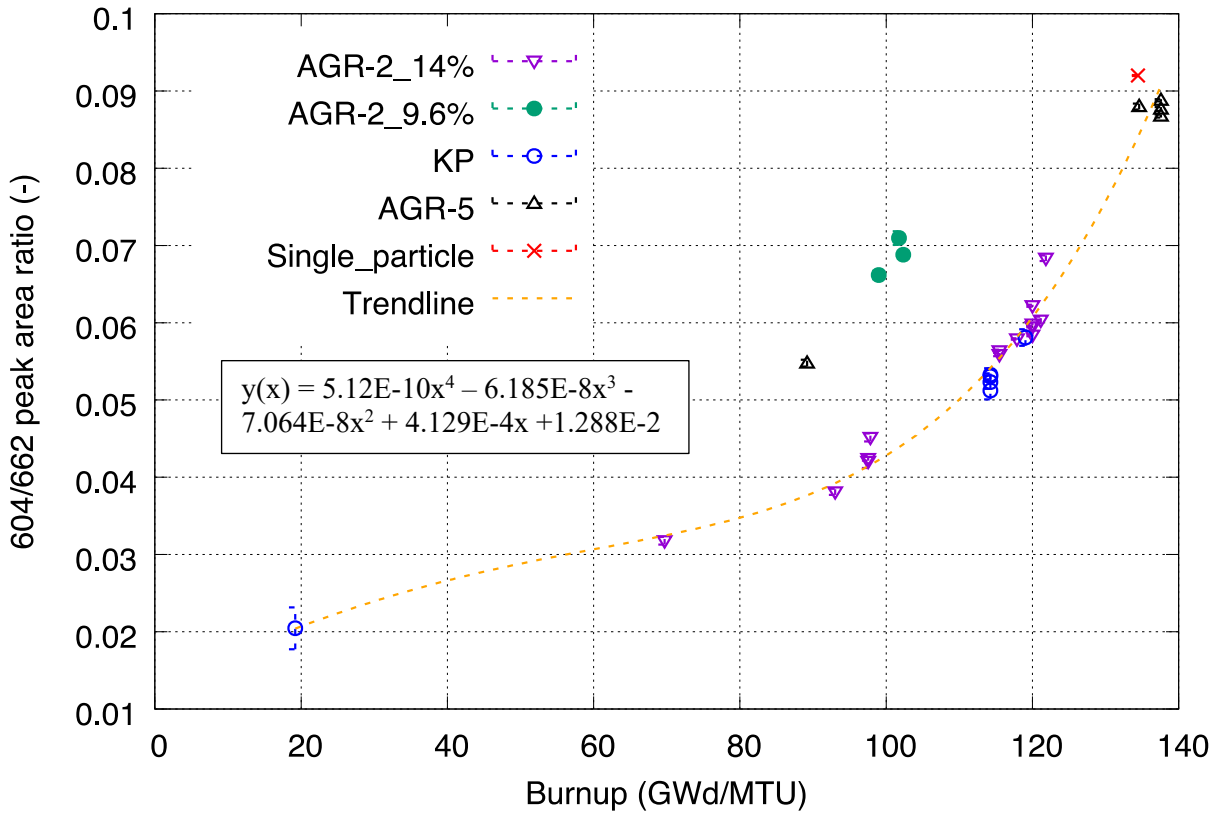

Figure 40. The 604/662 peak area ratios of the AGR vs. the samples' estimated burnups.

A few examples are offered in this subsection to compare the performance of the HPGe and the M400 detectors. Figure 41 compares the 662 keV peak area rate of the AGR-5-RS24 particle measured by the M400 and HPGe detectors vs. the standoffs. The 662 keV peak area rates of the HPGe were found to be 5–10× higher than those of the M400, indicating the higher detection efficiency of the HPGe detector.

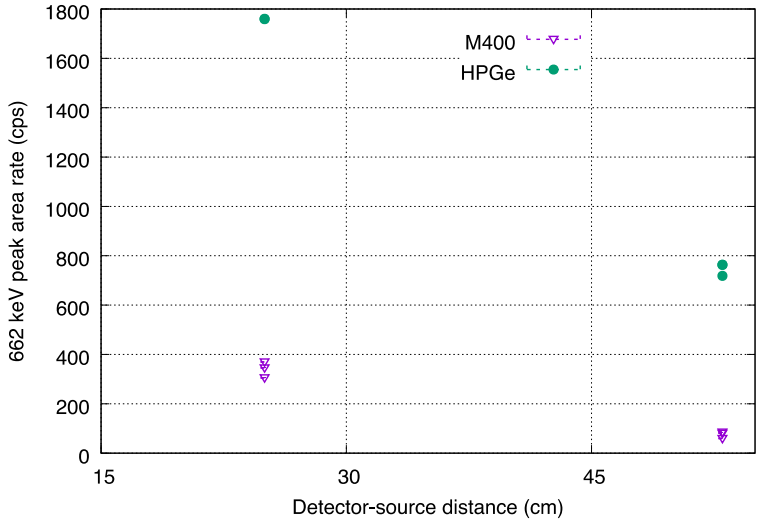

Figure 41. The measured 662 keV peak area rate of the AGR-5-RS24 particle by the M400 and HPGe detectors vs. the standoffs.

Similarly, Figure 42 compares the 662 keV peak area rate of all the AGR and KP samples measured at the hot cell by the M400 and HPGe detectors. Some samples were measured at several different standoffs, which explains multiple peak area rates for a given sample. Significantly higher peak area rates can be seen for the HPGe measurements, further demonstrating the HPGe's higher detection efficiency compared with the M400 detector.

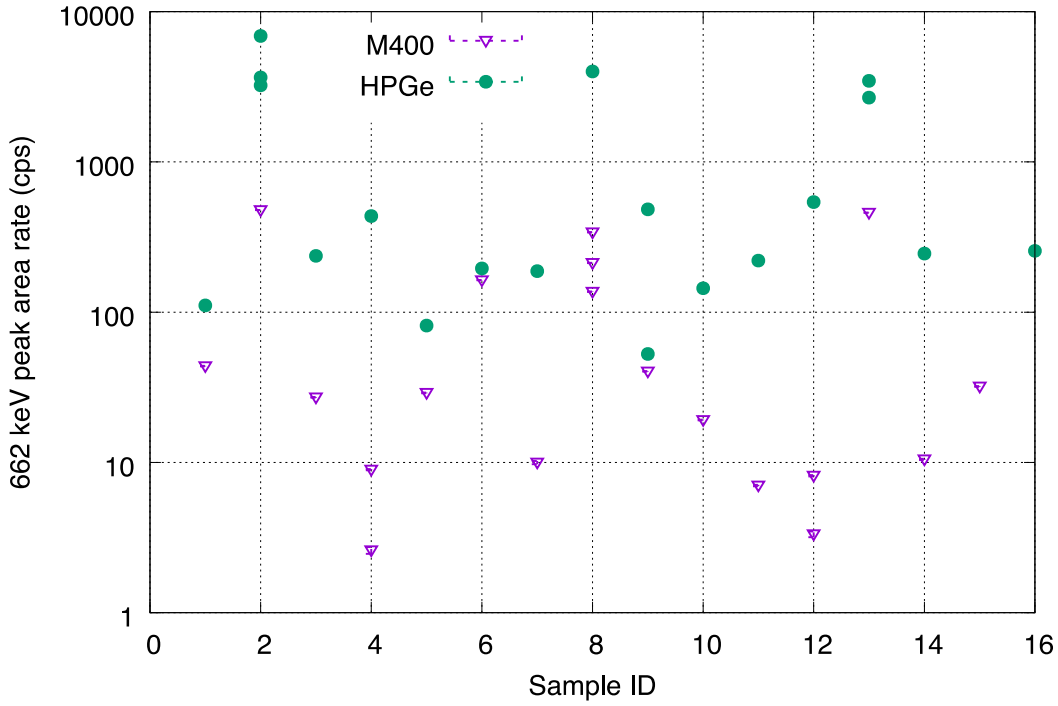

Figure 42. The 662 keV peak area rate of the AGR and KP samples measured by the M400 and HPGe detectors.

Figure 43 compares the 604/662 peak area ratios of the HPGe and the M400. A general positive trend can be seen between these two detectors, but there remain large scatters. Large error bars can be seen in some of the M400 results; they were associated with the weaker AGR sources, which led to lower count rates and thus larger error bars with the M400 detector. The error bars represent one sigma of the counting uncertainties.

However, the M400 detector appeared to be capable of withstanding higher gamma dose rates than the HPGe detector, as was expected owing to the pixelated nature of the M400 detector. Each pixel of the M400 detector has its own electric charge processing unit, whereas all charges deposited in the germanium crystal are processed together; the latter approach can lead to more pileups and thus poorer performance in a higher-dose-rate environment. To take the measurement of the AGR5-RS24 particle for an example, the dose rate at a 53-cm standoff was 1.8 mR/h based on the radiation control technician's measurement result, and the deadtime of the M400 was only 3% compared with 23% for the HPGe. At a 40-cm standoff where the dose rate was 3.2 mR/h, the deadtime of the M400 was 6%. At a 25-cm standoff where the dose rate was 8.2 mR/h, the deadtime of the HPGe was found to be 53%. For measurements of the AGR-5-223 compact (the highest dose-rate sample) through the collimator, the deadtime of the M400 was 12% at a standoff of 148 cm, whereas the deadtime of the HPGe was as high as 61% at a much longer standoff of 197 cm.

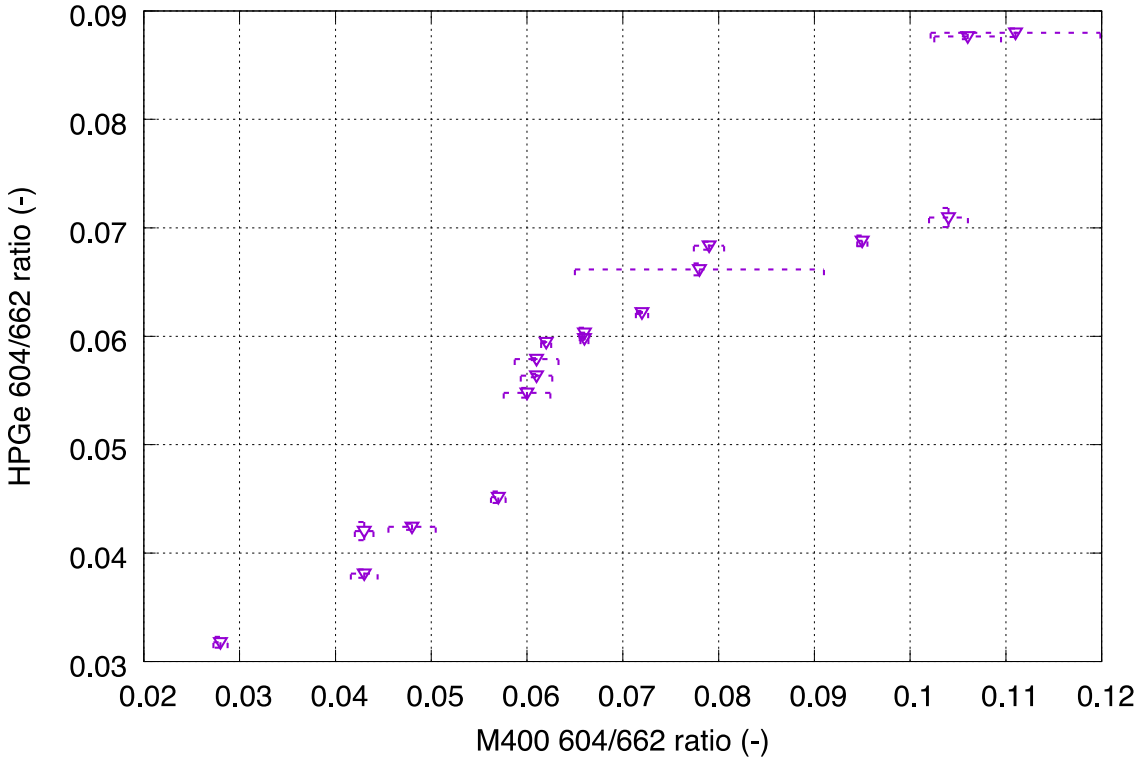

Figure 43. The measured 604/662 keV peak area ratios of the AGR and KP samples by the M400 and HPGe detectors.

4. MODELING OF THE GAMMA AND NEUTRON MEASUREMENTS

4.1 DEPLETION AND DECAY CALCULATIONS OF THE IRRADIATED TRISO FUEL SAMPLES

Depletion and decay calculations were performed in this work to generate the isotopic concentrations and the neutron and gamma source terms in the irradiated TRISO fuel samples, which were then fed into the MCNP and GADRAS models to simulate the neutron and gamma measurements. The AGR-2 and the AGR-5 samples were irradiated in the ATR at INL. Comprehensive depletion calculations, including following the complex power histories, have been performed at INL for the AGR program to simulate the irradiation of these samples using the JMOCUP code [12] [13]. With the help of an INL staff member [19], a subset of the JMOCUP results were retrieved, which include the concentrations, at one day after the irradiation, for a list of important isotopes such as ^{239}Pu, ^{240}Pu, ^{134}Cs, ^{137}Cs, ^{242}Cm, and ^{244}Cm. These concentrations were then loaded into ORIGEN to account for the decay time till the measurement date. Separate ORIGEN calculations used a generic PBR cross-section library to generate the concentrations for the remaining isotopes for the AGR samples, given that the ATR core model is not available to ORNL. For the KP samples, a cross-section library was generated using the 238-group neutron fluxes retrieved from the MCNP model developed for the KP sample irradiation in HFIR, which were then used in ORIGEN to simulate the depletion and decay of the KP samples to generate their isotopic concentrations and source terms.

4.2 GAMMA DETECTOR MODEL CALIBRATION

Gamma detector calibration was carried out using standard radioactive sources, specifically ^{137}Cs and ^{152}Eu, under controlled laboratory conditions. Accurate calibration is crucial, as it ensures the precision, reliability, and reproducibility of subsequent gamma spectroscopy measurements. These radioactive sources were selected because of their well-characterized gamma-ray emission energies and known intensity profiles, allowing for rigorous calibration of the detectors' energy scales and efficiency curves.

The ^{137}Cs source emits a well-defined gamma-ray peak at approximately 661.7 keV, making it particularly suitable for precise energy calibration and resolution verification of gamma detectors. On the other hand, ^{152}Eu emits multiple gamma-ray peaks spanning a broad energy range, from approximately 122 keV up to 1408 keV. This diverse energy profile allows for comprehensive detector efficiency calibration across a wide spectrum, making ^{152}Eu an invaluable calibration source for detailed gamma spectroscopy. Detector calibrations were systematically performed at two distinct source-to-detector distances: 20 cm and 53 cm.

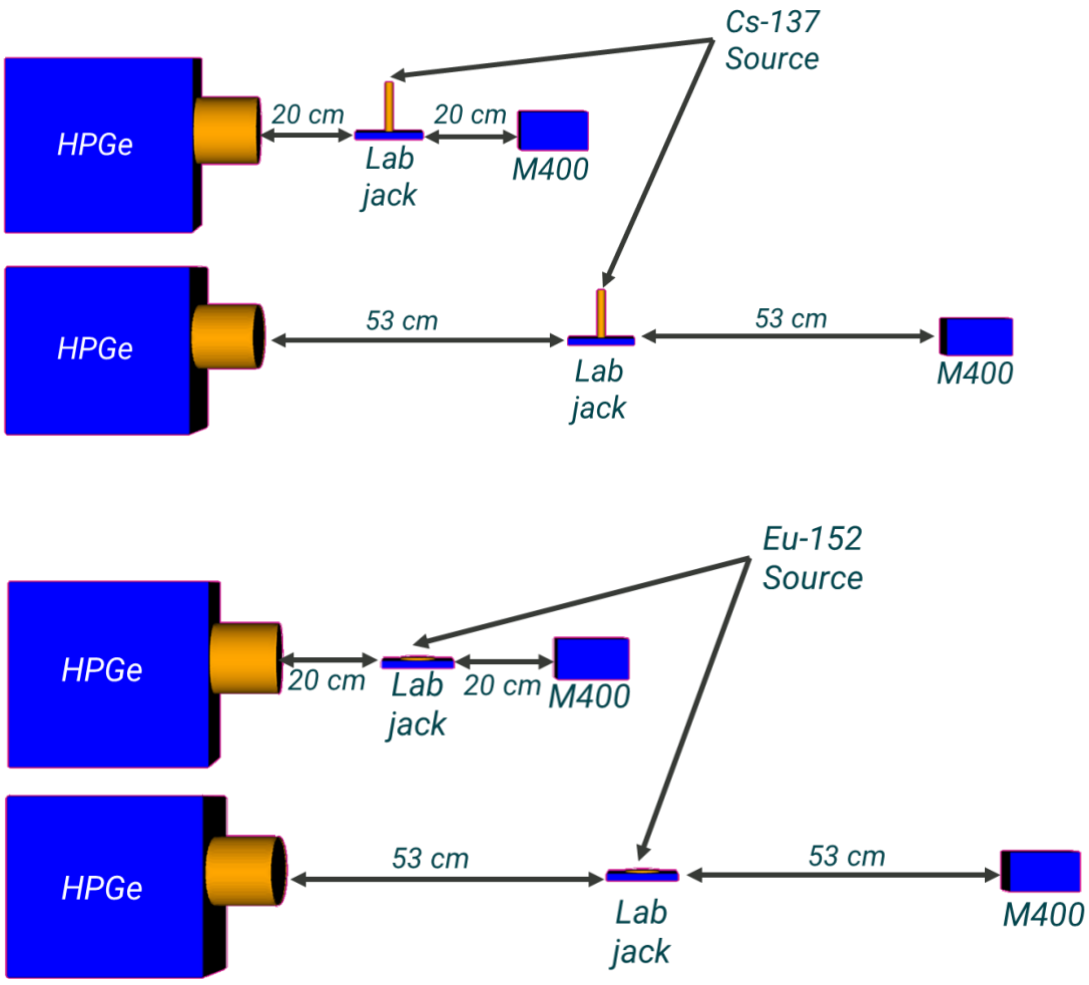

Figure 44. Simulation models for gamma detector calibration.

Additionally, to support and validate the experimental calibration measurements, detailed simulation models were developed using MCNP6.2. These MCNP simulations replicated the exact experimental setups for both radioactive sources and each detector configuration. Figure 44 presents the simulation geometries used in the MCNP models. The corresponding simulation results are provided in Figure 45, Figure 46, Figure 47, and Figure 48, clearly illustrating an excellent agreement between simulation predictions and experimental calibration measurements.

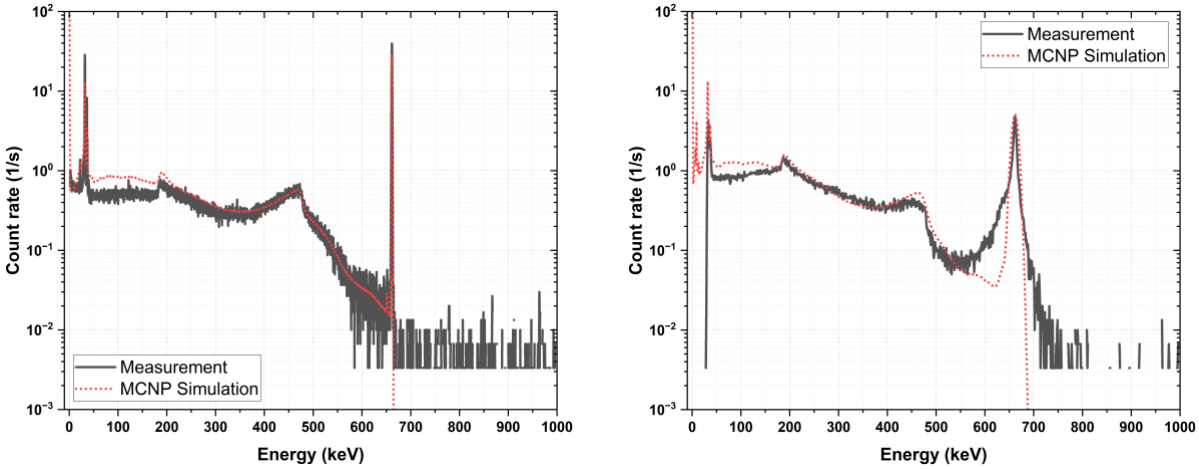

Figure 45. Gamma count rate from HPGe and M400 measuring ^{137}Cs source with distance 20 cm between detector and source.

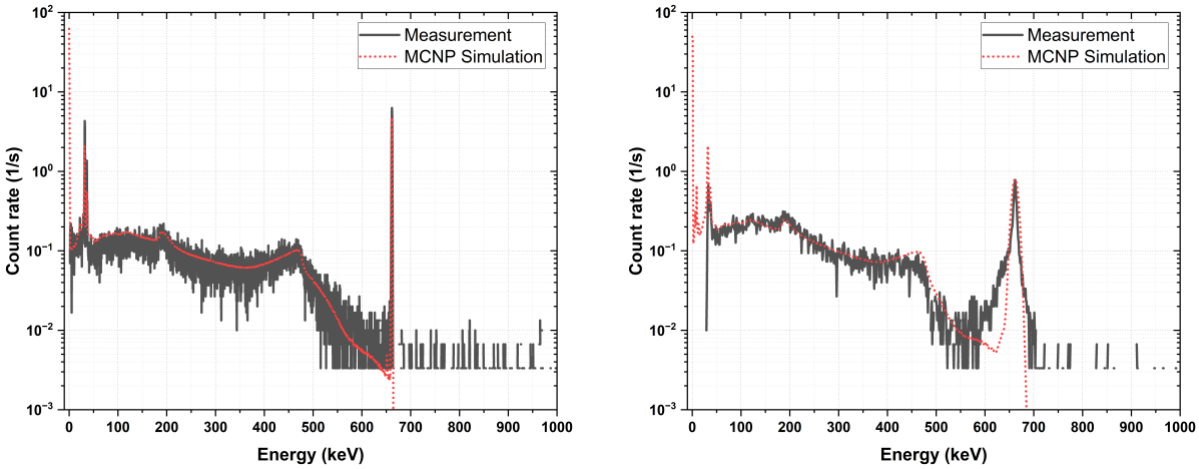

Figure 46. Gamma count rate from HPGe and M400 measuring ^{137}Cs source with distance 53 cm between detector and source.

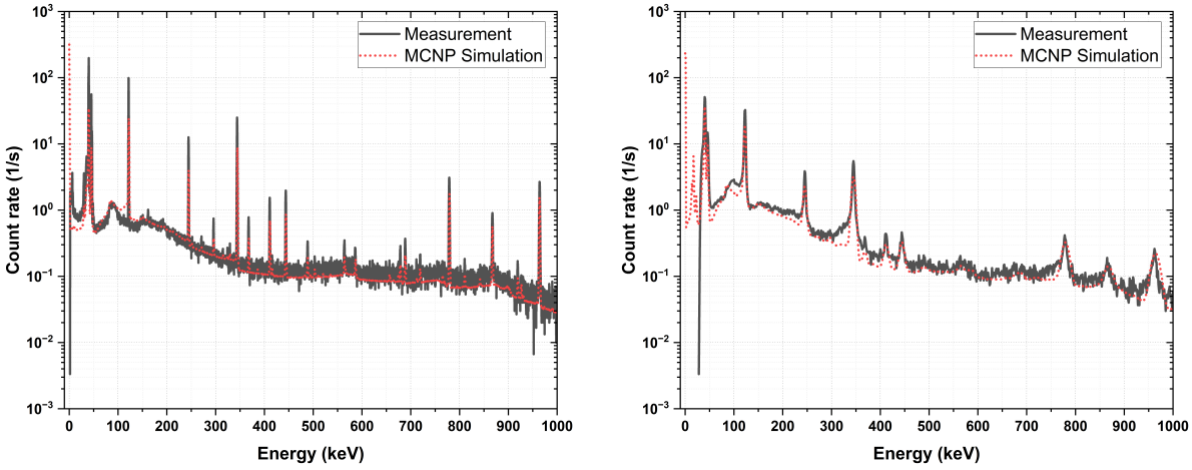

Figure 47. Gamma count rate from HPGe and M400 measuring ^{152}Eu source with distance 20 cm between detector and source.

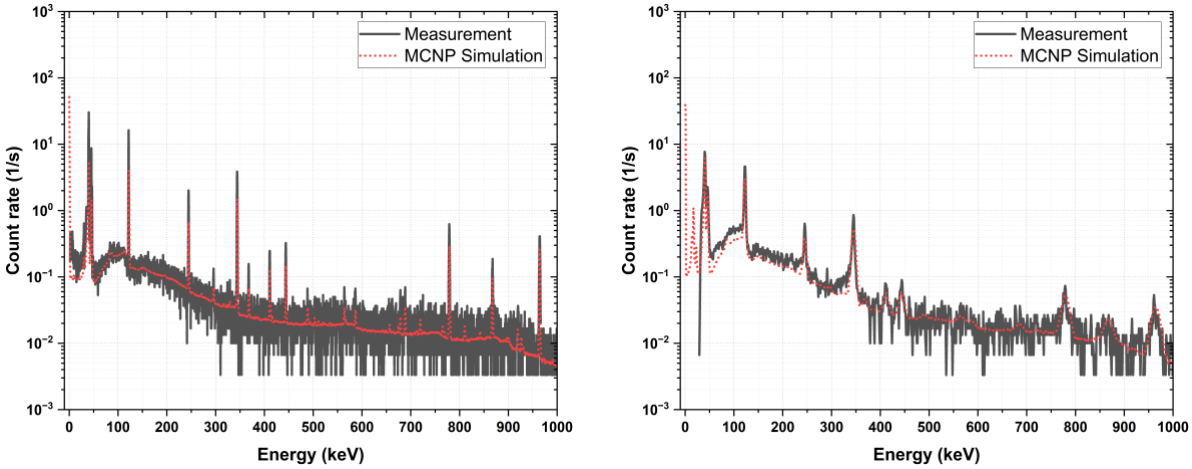

Figure 48. Gamma count rate from HPGe and M400 measuring ^{152}Eu source with distance 53 cm between detector and source.

4.3 GAMMA DETECTOR SIMULATION FOR IRRADIATED TRISO FUELS

4.3.1 MCNP Modeling and Simulation

Detailed simulation models were developed to support and validate the experimental gamma measurements of irradiated TRISO fuels using MCNP6.2. Figure 49 and Figure 50 illustrate the MCNP models developed specifically for the HPGe and M400 CZT detector setups, respectively. These simulation models closely replicated the experimental configurations, considering several detector-to-wall distances matching those used during the physical measurements. The photon emission sources for each irradiated TRISO sample were characterized and calculated using the SCALE/ORIGEN code to be used as the source terms in the simulations. To improve statistical accuracy, each MCNP simulation employed a large photon history of 1×10^{11} photons per second.

In these simulations, both the fuel samples and the detectors were modeled assuming idealized positioning, with each sample placed precisely at the center of the collimator slit and the detector aligned centrally relative to this slit. However, this assumption may not precisely reflect actual experimental conditions. During measurements, exact positioning of the irradiated samples within their stainless-steel canisters could not be visually verified owing to the limitations posed by the hot cell environment. As a result, in reality, slight deviations from the idealized central position of samples or detectors could introduce discrepancies between simulation results and experimental observations. Such deviations may explain some of the minor differences observed in direct comparisons of simulated and measured gamma-ray spectra and count rates.

Comparisons between the simulated gamma count rates and experimental measurements for various KP fuel samples are shown in Figure 51 through Figure 53. The bottom plot in Figure 52 further compares the simulated and measured gamma spectra of KP-125 in the energy range of 500 to 800 keV, where the simulated spectrum was scaled to match the measured 662 keV peak. The results demonstrate excellent overall agreement, confirming the accuracy and validity of both the MCNP modeling approach and the underlying assumptions regarding gamma emission spectra and detector geometry.

Figure 54 to Figure 58 further present the simulation results and corresponding experimental measurements for AGR samples measured in September 2023 and December 2023. While most of these results exhibit good alignment between simulation predictions and experimental data, certain comparisons reveal noticeable differences. These discrepancies are primarily attributed to measurement uncertainties

and the aforementioned assumptions related to exact sample and detector positioning. Nonetheless, the spectral shapes and characteristic gamma emission peaks identified in simulations closely match those observed experimentally, confirming the reliability of computational models.

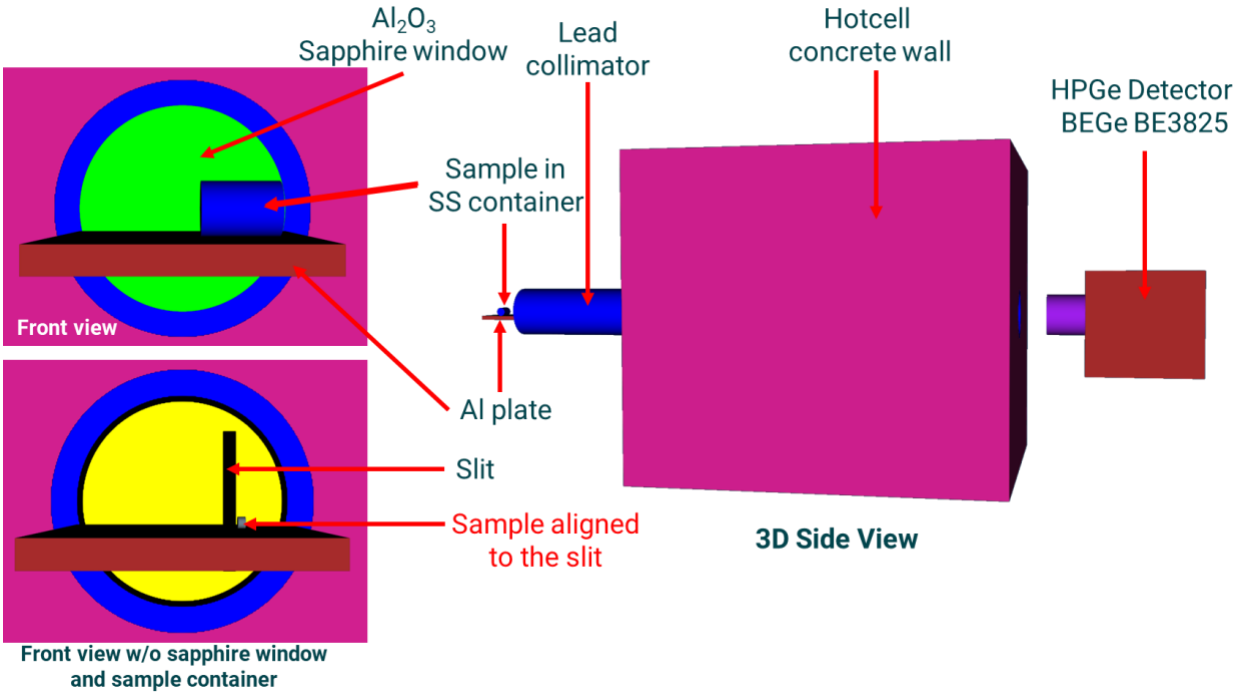

Figure 49. Simulation models for gamma measurement of irradiated TRISO fuels using HPGe.

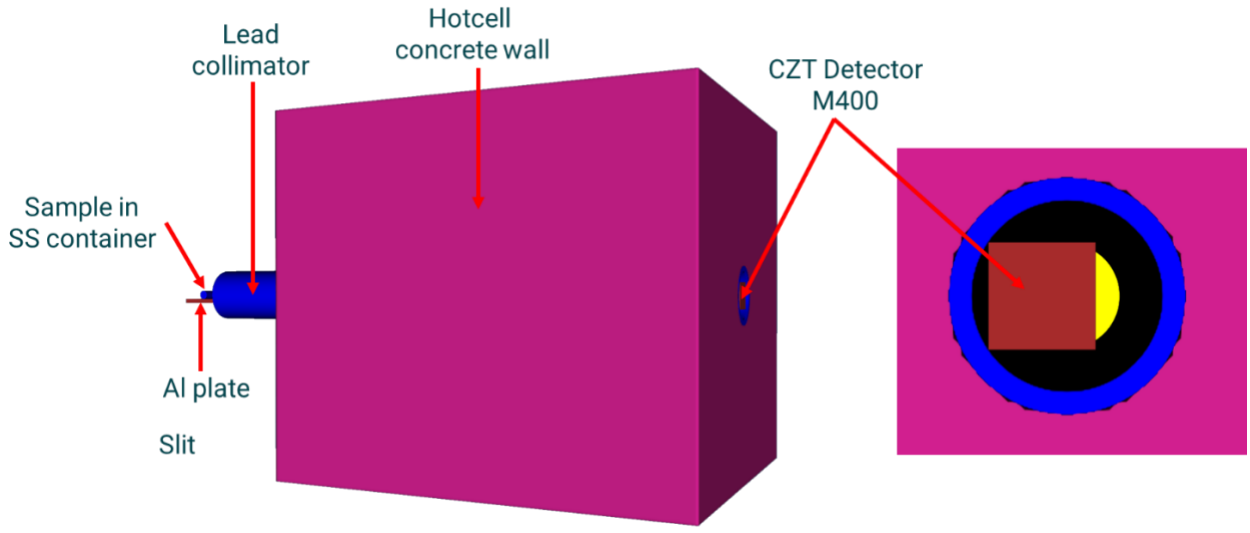

Figure 50. Simulation models for gamma measurement of irradiated TRISO fuels using CZT.

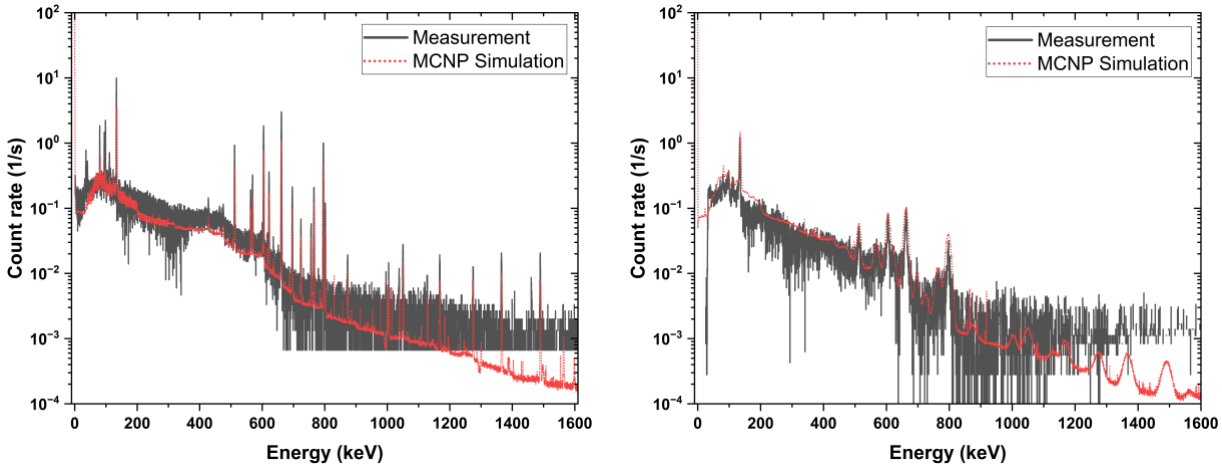

Figure 51. Simulation results of sample KP123 using (left) HPGe with distance of 2.75 in. between detector and hot cell wall and (right) CZT located inside the hot cell wall.

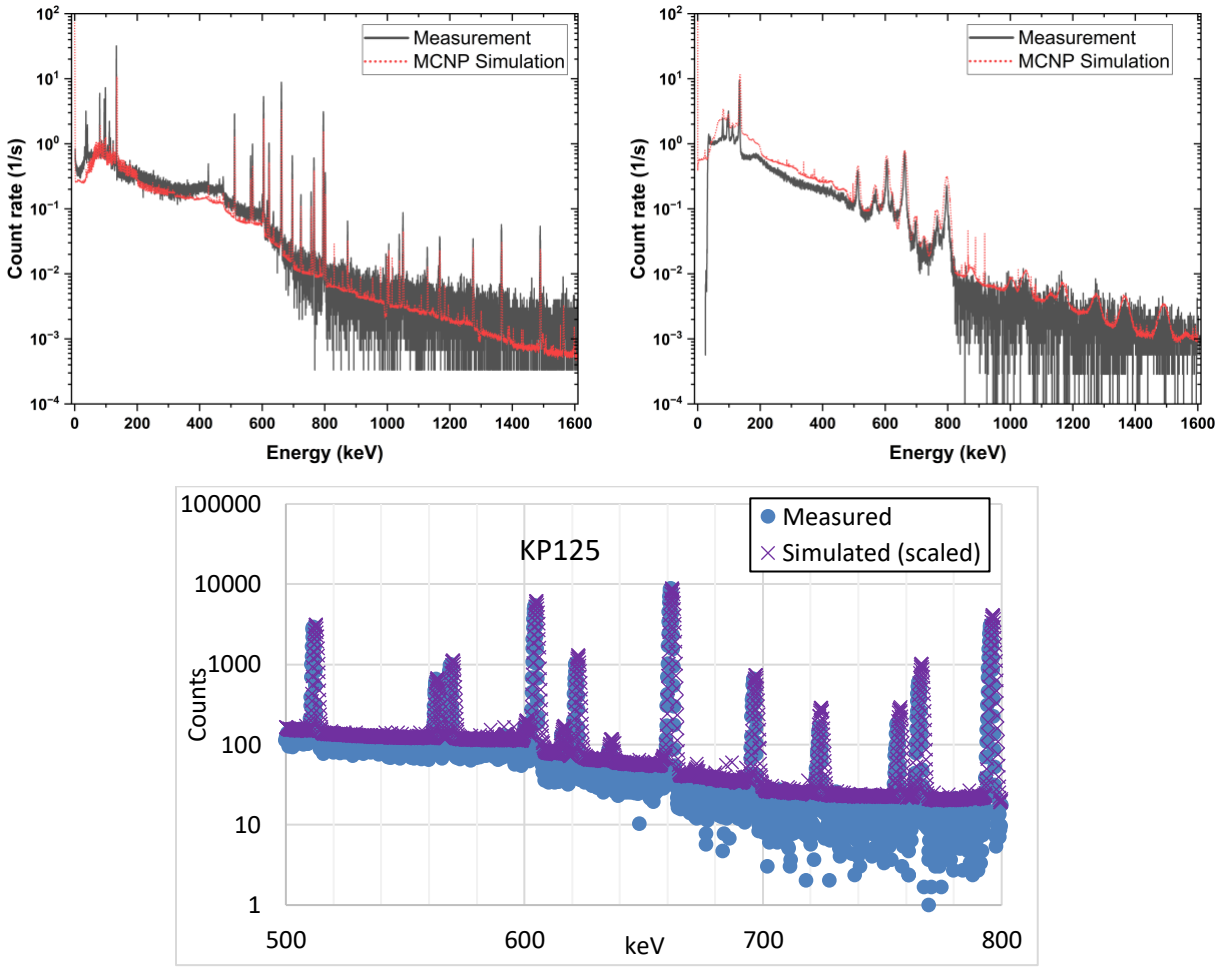

Figure 52. Simulation results of sample KP125 using (left) HPGe with distance of 2.75 in. between detector and hot cell wall and (right) CZT located inside the hot cell wall.

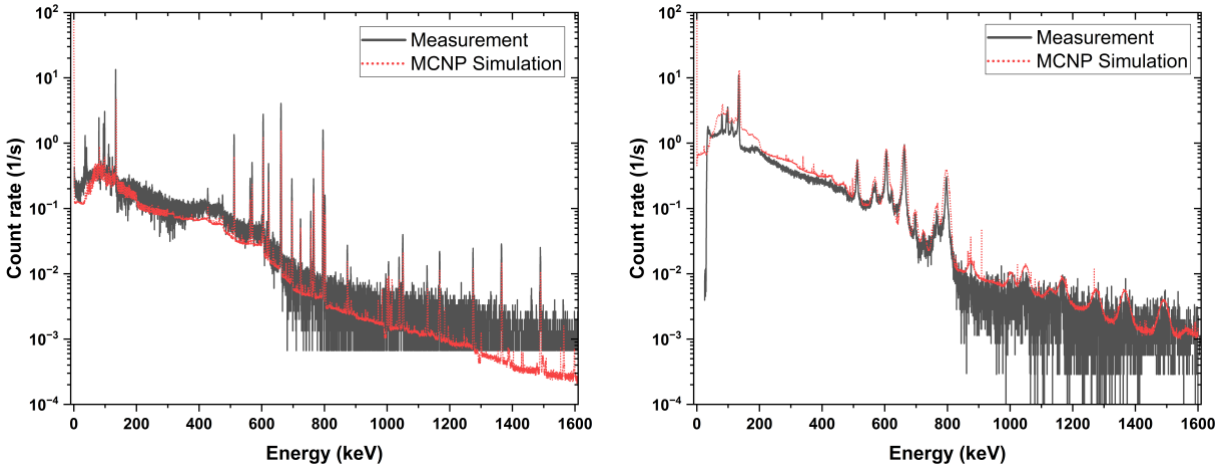

Figure 53. Simulation results of sample KP223 using (left) HPGe with distance of 2.75 in. between detector and hot cell wall and (right) CZT located inside the hot cell wall.

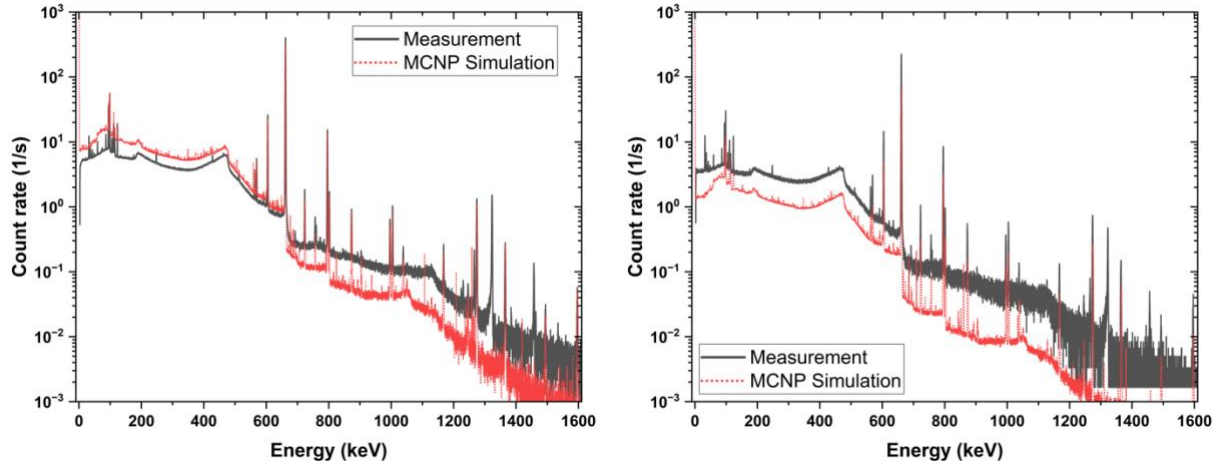

Figure 54. Simulation results of sample AGR2-221 measured in September 2023 using HPGe (left) located inside the hot cell wall and (right) with distance of 5.5 in. between detector and hot cell wall.

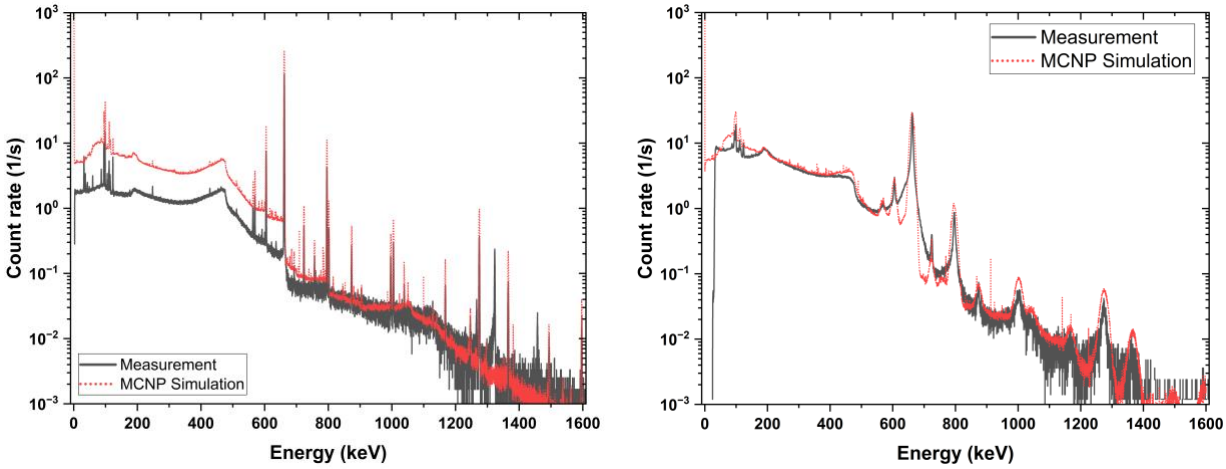

Figure 55. Simulation results of sample AGR2-221 measured in September 2023 using (left) HPGe with distance of 23.75 in. between detector and hot cell wall and (right) CZT with distance of 4.25 in. between detector and hot cell wall.

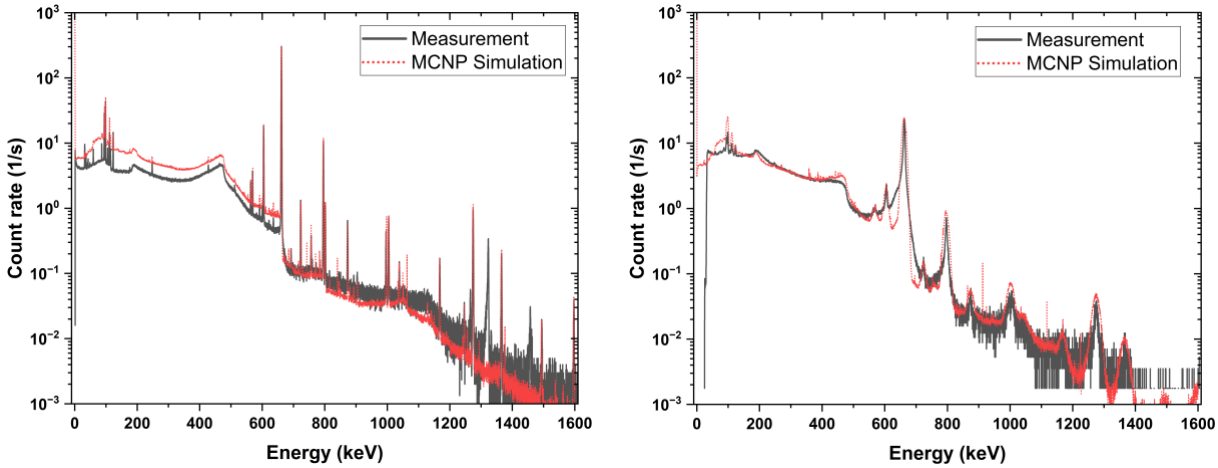

Figure 56. Simulation results of sample AGR2-221 measured in December 2023 using (left) HPGe with distance of 38.25 in. between detector and hot cell wall and (right) CZT located inside the hot cell wall.

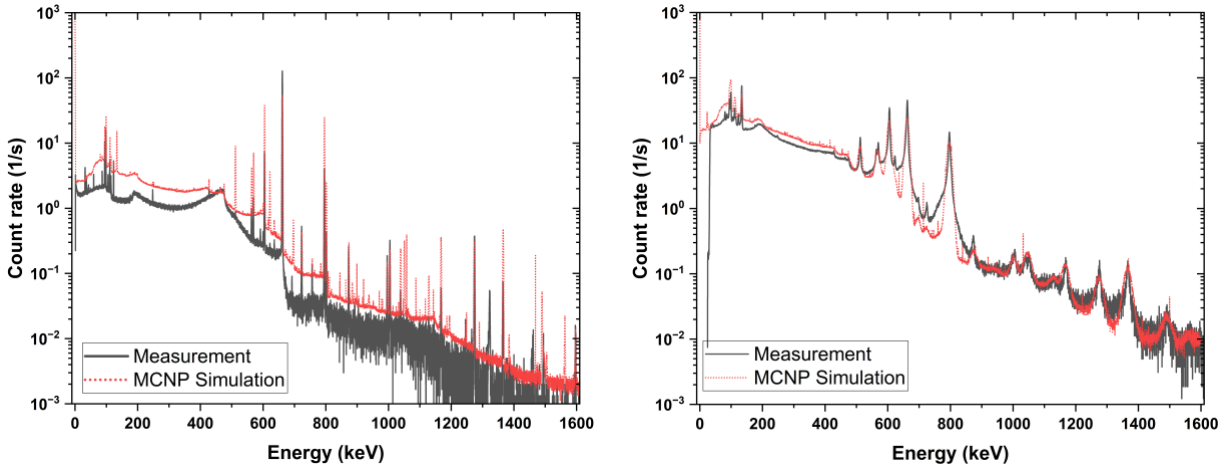

Figure 57. Simulation results of sample AGR5-223 measured in September 2023 using (left) HPGe with distance of 23.75 in. between detector and hot cell wall and (right) CZT with distance of 4.25 in. between detector and hot cell wall.

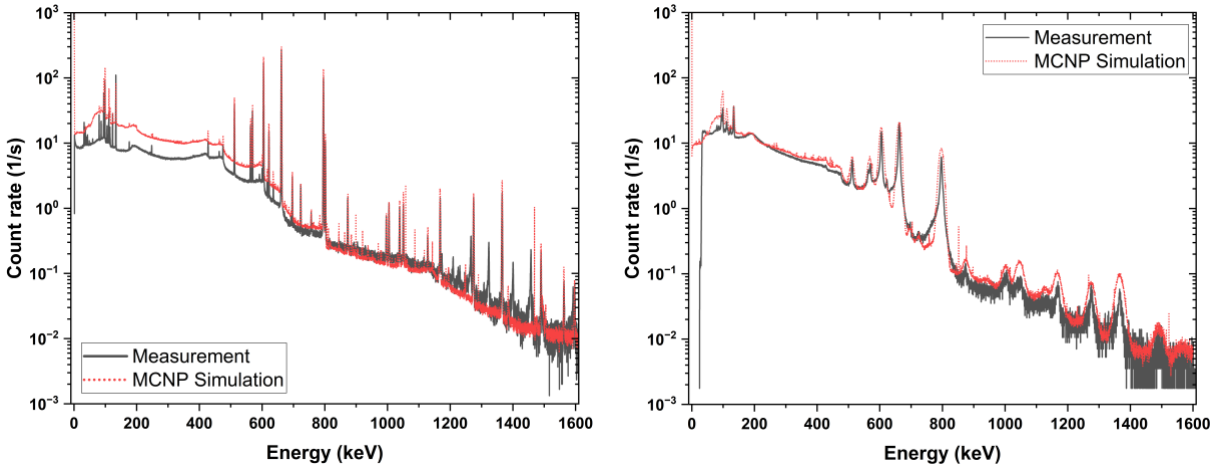

Figure 58. Simulation results of sample AGR5-223 measured in December 2023 using (left) HPGe with distance of 38.25 in. between detector and hot cell wall and (right) CZT located inside the hot cell wall.

4.3.2 GADRAS Modeling and Simulation

GADRAS modeling was also performed to cross-check the MCNP modeling results, as it takes less time to build and run a GADRAS model than an MCNP model. Custom detector files were first developed using the specifications provided by Mirion for the HPGe detector used in this work. The parameters of these detector files were then optimized by the specs and the measured spectra of the ^{137}Cs and ^{152}Eu source standards, which are essentially point sources. Figure 57 shows the user interface for setting up the custom detector files. The boxes under "Dimensions" show the specs of the HPGe provided by Mirion, which were kept as constants during the optimization. The boxes with yellow background show the parameters that have been optimized to match the measured ^{137}Cs and ^{152}Eu HPGe spectra.

Figure 60 and Figure 61 compare the measured and GADRAS-simulated HPGe spectra of the ^{137}Cs and ^{152}Eu source standards, respectively. Generally good agreements can be seen, with all major peaks aligned between the measured and simulated results, although discrepancies exist in the magnitudes of many peaks. These GADRAS results are similar to the MCNP results shown in Figure 45, Figure 46, Figure 47,

and Figure 48, demonstrating that GADRAS with customized detector files has similar performance for point gamma sources.

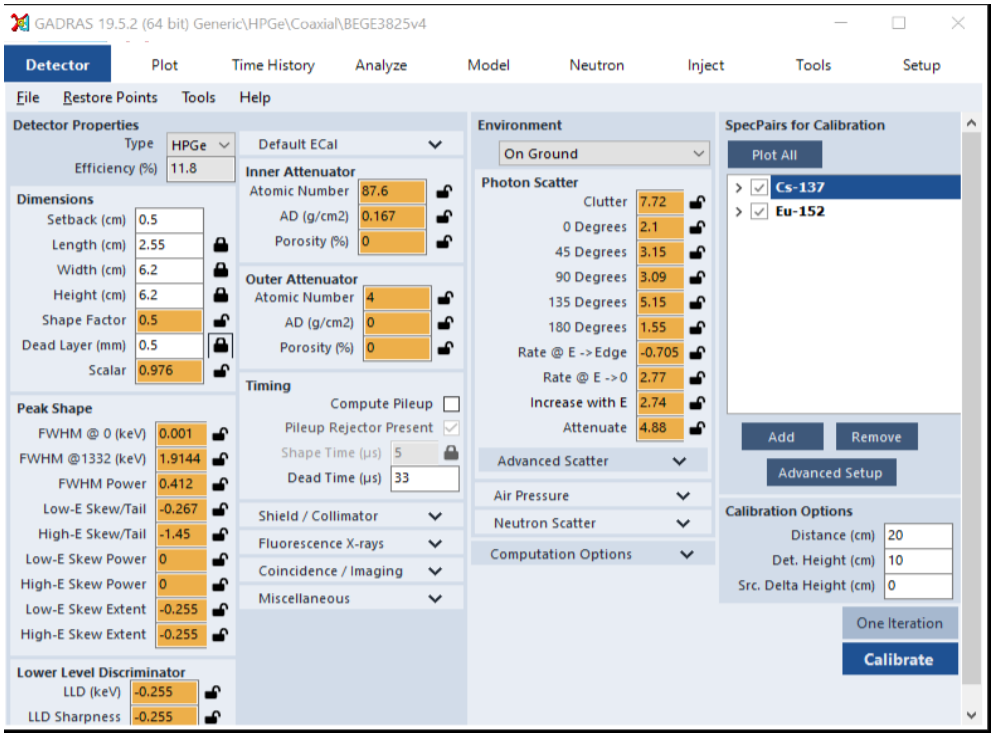

Figure 59. A GADRAS user interface showing the parameters shown in yellow background that have been optimized to match the measured ^{137}Cs and ^{152}Eu HPGe spectra.

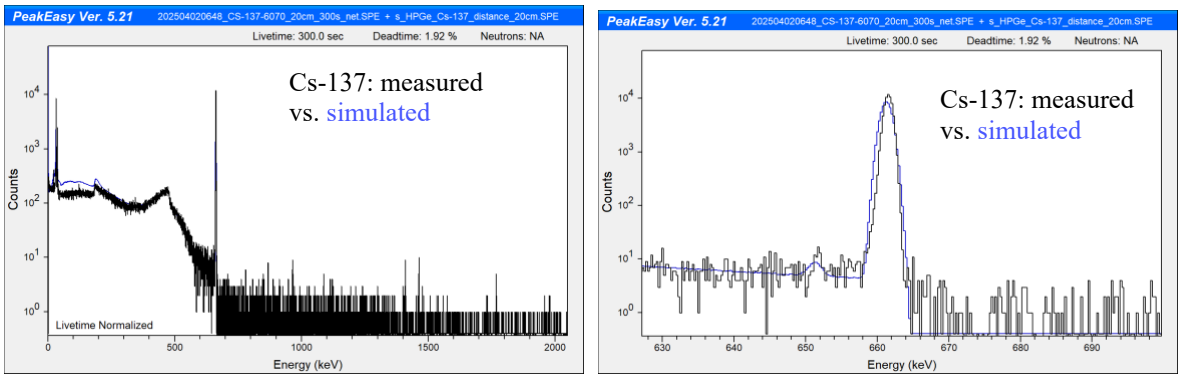

Figure 60. (Left) Comparison of the HPGe gamma spectra of the ^{137}Cs source standard: measured vs. simulated by GADRAS (blue); (right) zoomed in the [500, 900] keV range.

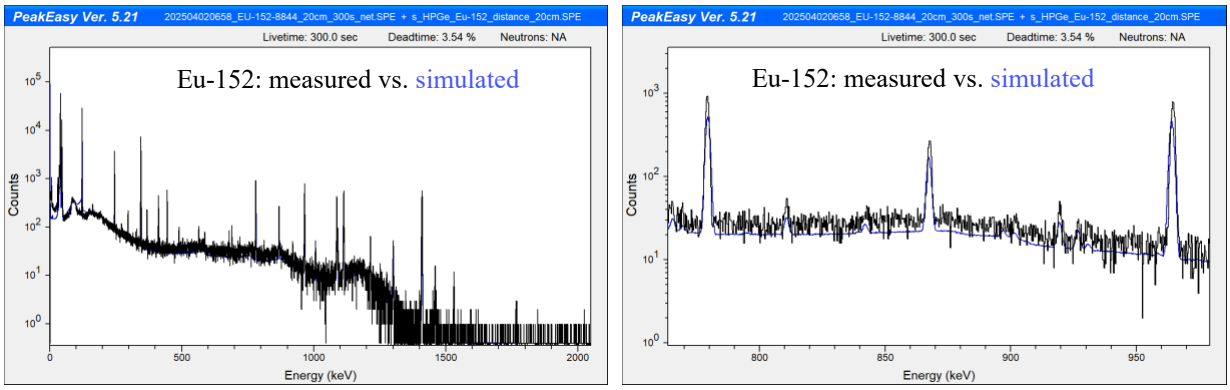

Figure 61. (Left) Comparison of the HPGe gamma spectra of the ^{152}Eu source standard: measured vs. simulated by GADRAS (blue); (right) zoomed in the [500, 900] keV range.

GADRAS models were developed to simulate the HPGe measurements for an irradiated TRISO particle and for an irradiated TRISO compact. Figure 62 shows the GADRAS model of a TRISO particle on the left, with the kernel and each of the coating layers explicitly modeled. It shows the model of a TRISO compact on the right, with the container included. The mixture of TRISO particles and the graphite matrix of the compact was homogenized for simplification. The gamma radiation source terms were generated by GADRAS by feeding the comprehensive nuclide concentrations of nuclear materials contained in both models, which were results of depletion and decay calculations of the TRISO samples described in Subsection 4.1.

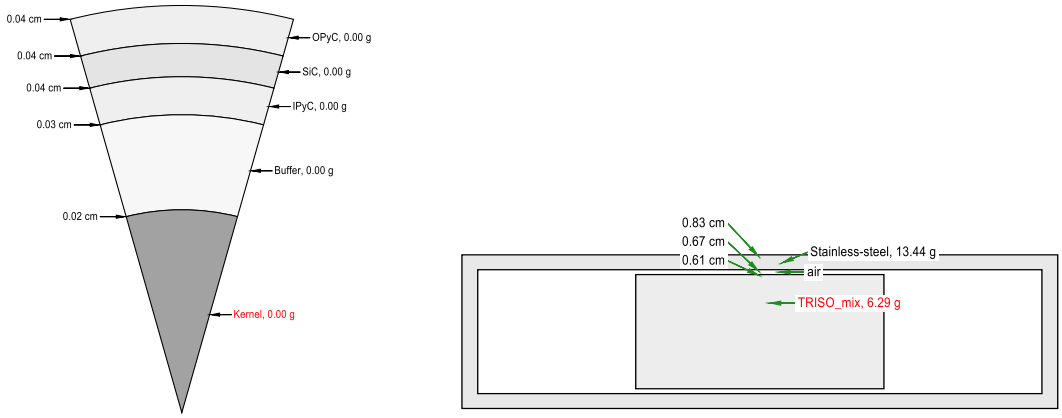

Figure 62. (Left) The GADRAS model of a TRISO particle; (right) The GADRAS model of a TRISO compact.

Figure 63 compares the measured and GADRAS-simulated HPGe gamma spectra of the AGR-2-XR143 particle, with the left figure showing the simulated results using the customized detector file mentioned earlier and the right figure showing the simulated results using the built-in detector file for a generic 95% HPGe. The GADRAS results shown in the left figure somewhat resemble the MCNP results shown in Figure 54, both of which show close agreement between the measured and simulated results before the 662 keV peak and large discrepancies after that peak (shown as significant drop-offs in the continuum). Similar deteriorations after the 662 keV peak are seen in the MCNP results shown in Figure 55. However, such deteriorations are not shown in the right figure of Figure 63 when a generic GADRAS detector file was used. These results suggest that the specifications of the HPGe detector provided by Mirion either were inaccurate or did not fully capture the intrinsic features of this detector, which is a subject of future investigation.

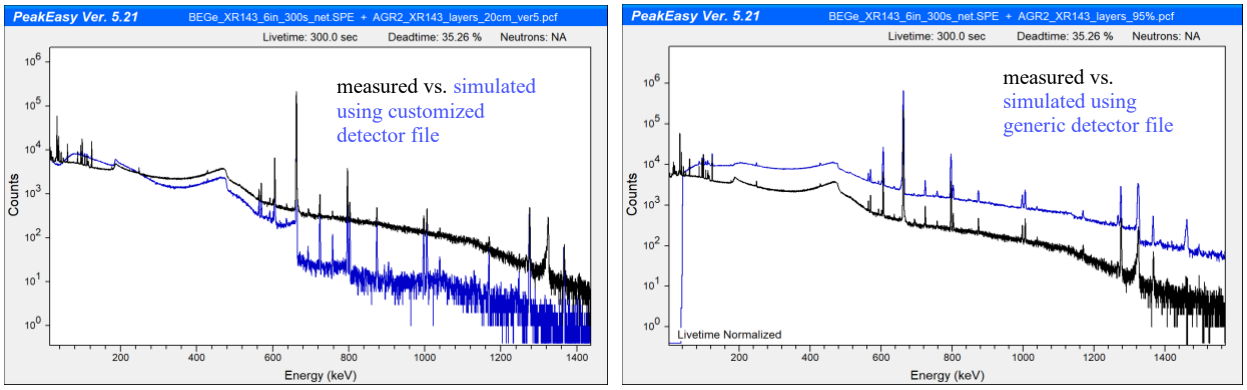

Figure 63. Comparison of the HPGe gamma spectra of the AGR-2-XR143 particle: measured vs. simulated by GADRAS (blue); (left) using the customized detector files for the HPGe used in the measurements; (right) using the built-in detector files for a generic 95% HPGe detector.

Figure 64 compares the measured and GADRAS-simulated HPGe gamma spectra of the AGR-2-211 compact, which was measured through the collimator in the hot cell. Given that GADRAS does not have a way to model a collimator, the collimator used in the measurement was not modeled in this model. Without accounting for the collimator, the simulated results were expected to be much higher than the measured results because the shielding and attenuation effects were not accounted for in the simulation. Therefore, the simulated results shown in the left figure were multiplied by a factor 0.00094 and a factor of 0.0011 in the right figure. The goal of this figure was to compare the shapes of simulated spectrum with the measured one. Somewhat close agreements in spectrum shapes are seen in this figure, which resembles the MCNP results shown in Figure 54. These results show that GADRAS can be used to simulate spectra with a collimator if a multiplication factor is used, which can be derived using measurements of point source standards.

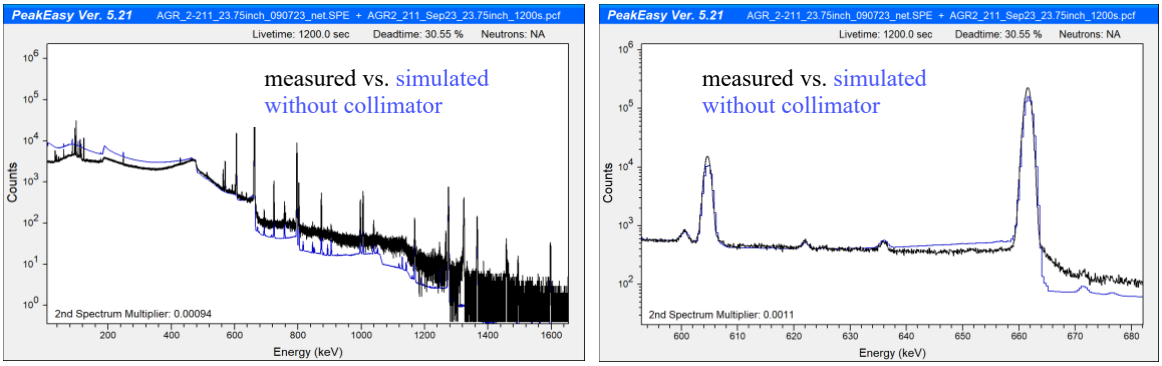

Figure 64. (Left) Comparison of the HPGe gamma spectra of the AGR-2-211 compact: measured vs. simulated by GADRAS (blue); (right) zoomed in the [500, 900] keV range. Note that multiplication factors of 0.00094 and 0.0011 have been applied to the simulated spectra in the left figure and the right figure, respectively.

4.4 QUANTITATIVE COMPARISON BETWEEN MEASURED AND SIMULATED GAMMA SPECTRA

In addition to the qualitative comparisons presented in the previous two subsections between the simulated and measured gamma spectra of these irradiated TRISO fuel samples, some quantitative comparisons are presented in this subsection. Figure 65 shows the simulated-to-measured (S/M) ratios of the three Cs peak areas vs. burnup among the irradiated TRISO fuel samples. In this comparison, the simulated peak area of a particular peak (e.g., 662 keV) was compared with the corresponding measured

peak area, resulting in the S/M ratio. A perfect match is achieved if the S/M equals 1.0. Although a subset of the data points fluctuates in a relatively small range about 1.0, large scatters are seen among these ratios; these can be attributed to the complexity of the gamma source terms in the various irradiated TRISO samples and the measurements themselves (e.g., the alignment issues through the slit in the collimator). Figure 66 shows the S/M ratios of the 604/662 peak area ratios vs. burnup among the irradiated TRISO fuel samples. In this comparison, the simulated 604/662 peak area ratios of a particular measurement were compared with the corresponding measured 604/662 peak area ratio, resulting in the S/M ratio. Compared with Figure 65, Figure 66 shows a much smaller range in the S/M ratios among the TRISO samples, highlighting the benefit of using peak ratios instead of absolute peak areas owing to the uncertainty cancellation effects in the peak ratio. On average, there was an ~10% overprediction in ratios derived from the simulated spectra relative to the ratios from measured spectra. Such overprediction could be mitigated if there were a large number of repeated measurements in a fixed measurement configuration, which is the case for gamma measurements of the pebbles at the burnup monitor station shown in Figure 2 and Figure 3.

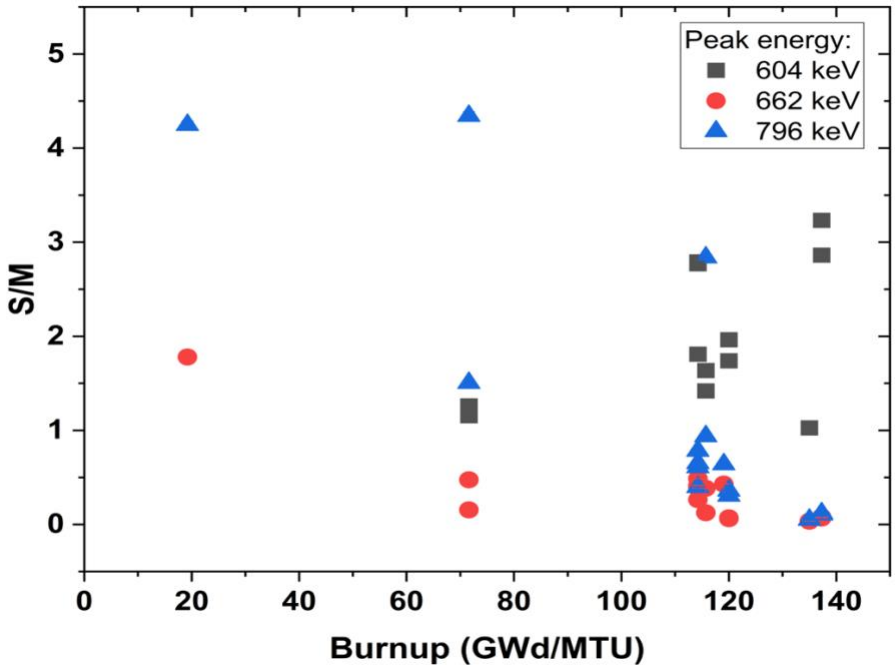

Figure 65. The simulated-to-measured (S/M) ratios of the three HPGe Cs peak areas vs. burnup among the irradiated TRISO fuel samples.

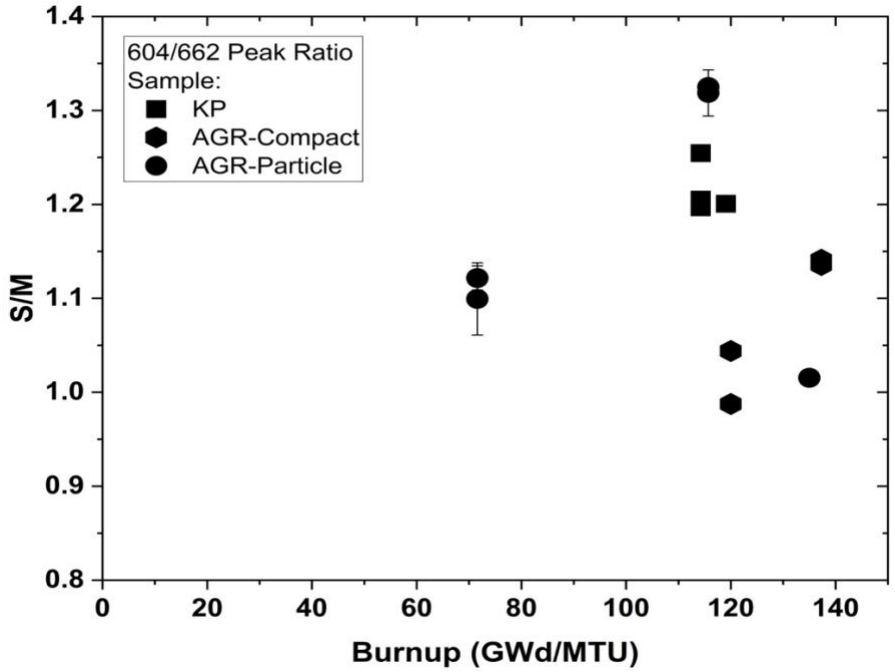

Figure 66. The S/M ratios of the HPGe 604/662 peak area ratios vs. burnup among the irradiated TRISO fuel samples.

4.5 NEUTRON DETECTOR CALIBRATION

Calibrations of both the Makeshift and VPMC neutron detectors were performed using standard ^{252}Cf sources. The ^{252}Cf source denoted by CF6081 was used for the Makeshift calibration measurements, and the ^{252}Cf source denoted by CF3409 was used for VPMC measurements because of the source availability at the time. The neutron emission rates of the CF6081 and CF3409 sources were determined to be 60785 and 672.5 n/s, respectively, at the respective dates of these calibration measurements based on the Shuffler measurement data and source certificate.

MCNP6.2 was used to develop detailed models to simulate these calibration measurements, which are illustrated in Figure 67 for the Makeshift detector and in Figure 68 for VPMC. The corresponding simulation result is provided in Table 5. Less than 4% discrepancies were observed between the measured and simulated neutron count rates for both detectors, demonstrating the validity of the respective MCNP models.

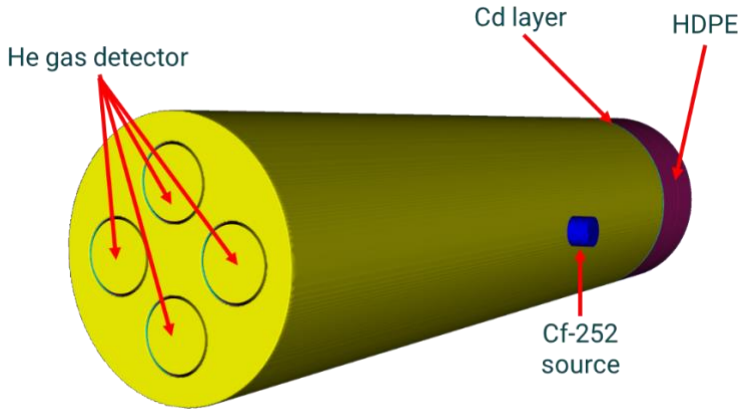

Figure 67. MCNP models of the ^{252}Cf calibration measurement of the Makeshift detector.

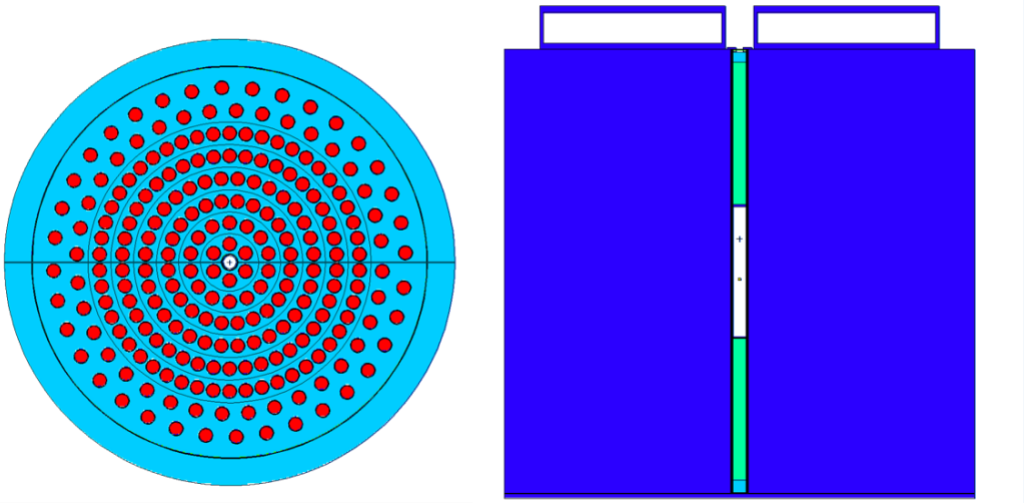

Figure 68. MCNP models of the ^{252}Cf calibration measurement of the VPMC detector.

Table 5. Simulation results for makeshift neutron detector calibration

Detector	Type	Count rate (n/s)
Makeshift	Measurement	765.43
	Simulation	762.85
VPMC	Measurement	510.91
	Simulation	529.52

4.6 NEUTRON DETECTOR SIMULATION FOR IRRADIATED TRISO FUELS

Detailed models were also developed to simulate the neutron measurements of irradiated TRISO fuel samples using the MCNP6.2. Figure 69 presents the MCNP models for the Makeshift detector measurements of the AGR5-223 and KP-125 samples in the hot cell. The neutron emission sources for each irradiated TRISO sample were calculated using the depletion and decay calculations described in Subsection 4.1 and they were fed into the MCNP models. To improve statistical accuracy, each MCNP simulation was run with 1×10^{11} of neutron histories. The simulation neutron count rates for both TRISO

samples are summarized in Table 6. However, large discrepancies between the simulated and measured rates were observed, which can be primarily attributed to the high neutron backgrounds in the hot cell as described in Subsection 2.4. Uncertainties in the source terms and measurement alignments also can contribute to the discrepancies. Table 7 summarizes the MCNP simulation results for the VPMC measurements of the irradiated TRISO particles at the SEL. Large discrepancies between the simulated and measured count rates were also observed, which can be primarily attributed to the low neutron emission rates in the individual TRISO particles that were much lower than the background neutrons owing to various sources stored at the SEL. Uncertainties in the source terms and measurement alignments also may contribute to the discrepancies.

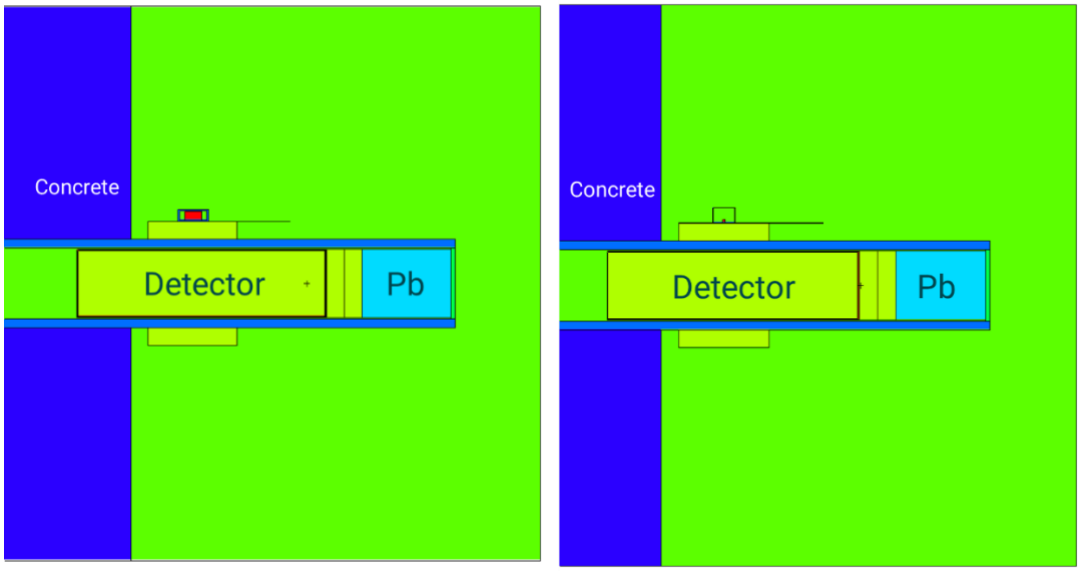

AGR5-233 sample **KP-125 sample**

Figure 69. Simulation models using makeshift neutron detector during hot cell measurement of irradiated TRISO fuels.

Table 6. Measurement and simulation results using makeshift neutron detector during hot cell measurement of irradiated TRISO fuels.

Compact ID	Measurement (n/s)	Simulation (n/s)
AGR5-223	2.3 ± 0.5	14.940 ± 0.003
KP125	3.1 ± 0.5	0.006 ± 0.003

Table 7. Measurement and simulation results using VPMC of irradiated TRISO fuels.

Sample ID	Measurement (n/s)	Simulation (n/s)
AGR2-XR136	0.215 ± 0.102	0.0087 ± 0.000
AGR2-XR143	0.182 ± 0.116	0.0687 ± 0.000

5. SUMMARY AND CONCLUSIONS

Given the unique characteristics of the PBR fuel cycle, both gamma and neutron measurements are expected to play important roles in performing and maintaining nuclear MC&A for spent pebbles to safeguard the fuel cycle. Given the lack of irradiated pebbles in the United States, a variety of irradiated TRISO fuel samples with wide ranges of burnups and cooling times available at ORNL were used in this work. A large number of gamma and neutron measurements were performed on these samples to collect data to test the various detectors and to benchmark the computer models used to simulate the depletion and decay of the fuel and the measurements themselves.

A neutron detector was designed and fabricated using available hardware and was made to fit inside the existing collimator in the hot cell wall to measure the irradiated TRISO fuel samples in the hot cell. The measurements were impacted by the high neutron background from various spent PWR fuel rodlets scattered inside the hot cell, but significant improvements were obtained after several steps were taken to reduce the background counts. Meaningful neutron count rates were obtained for two samples in the end. The high-efficiency VPMC detector, developed for a previous NA-22 project, was used to measure the individual irradiated TRISO particles in a lab. The net count rates were found to be low relative to the high background neutrons from various sources stored in the lab. Large discrepancies were observed between the simulated and measured neutron count rates of both detectors, primarily owing to the relatively higher background counts in these measurements. However, close agreements were observed between the simulated and measured neutron count rates in both detectors' measurements of californium calibration sources, which demonstrated the validity of the respective MCNP models of each neutron detector. An irradiated/spent pebble will be a much stronger neutron source than the irradiated TRISO samples measured in this work; many of the challenges faced in this work will be alleviated when pebbles are measured using these detectors.

For the gamma measurements, three different gamma detectors were used, including a broad-energy HPGe detector, an M400 CZT detector, and a NaI detector. The M400 was recently adopted by the IAEA for fresh uranium measurements, but it has not been tested for spent fuel measurements before this project. As expected, the HPGe had much superior energy resolutions than the other two detectors. The M400 detector has much better energy resolutions than the NaI detector, representing significant performance improvements in M400 over a conventional room-temperature detector. Both the HPGe and M400 detectors were able to measure the 604 and 662 keV peaks from these samples, which are the two most important peaks used to infer fuel burnup. Although the energy resolution of the M400 detector was not nearly as good, and it did not detect some of the minor peaks as the HPGe detector, it was found to be capable of handling significantly higher dose rates than the HPGe. Trending analysis shows that the M400 detector was able to measure the 604/662 peak ratios with accuracies somewhat close to that of the HPGe detector, except for a few weak TRISO samples. Given the complexities in the TRISO samples (e.g., different sample sizes) and uncertainties in the alignments between the detector and the TRISO fuel inside the containers, large scatters were found between the peak area rates and the sample burnups. However, the 604/662 peak ratios were found to trend well with the sample burnups among most samples in both measured and simulated results. Such scatters are expected to be smaller when it comes to the gamma measurement of the spent pebbles because there will be a large number of repeated measurements in a fixed configuration.

These measurement data will be shared with the safeguards community so that they can be used to benchmark users' own models. They will also be used to inform uncertainties in the pebble data tool under development to assist the MC&A of spent pebbles.

6. REFERENCES

[1] "Xe-100: The Most Advanced Small Modular Reactor," [Online]. Available: https://x-energy.com/reactors/xe-100. [Accessed July 2025].

[2] P. C. Durst et al., "Nuclear Safeguards Considerations for the Pebble Bed Modular Reactor (PBMR)," INL, INL/EXT-09-16782, Idaho Falls, ID, 2009.

[3] C. Mao, Y.-B. Liu and L.-G. Zhang, "Application of Anticoincidence Technology to Burn-Up Measurement Systems in High-Temperature Gas-Cooled Reactors," *Sustainability,* vol. 10, no. 8, p. 2883, 2018.

[4] H. Menlove, S. Menlove and S. Tobin, "Fissile and Fertile Nuclear Material Measurements using a New Differential Die-Away Self-Interrogation Technique," *Nuclear Instruments and Methods in Physics Research Section A: Accelerators, Spectrometers, Detectors and Associated Equipment,,* vol. 602, no. 2, pp. 588-293, 2009.

[5] T. Lee, H. Menlove, M. Swinhoe and S. Tobin, "Differential Die-Away Technique for Determination of the Fissile Contents in Spent Fuel Assembly," in *INMM 51st Annual Meeting*, Baltimore, Maryland, USA, July 11-15, 2010.

[6] V. Henzl, M. Swinhoe, S. Tobin and H. Menlove, "Measurement of the Multiplication of a Spent Fuel Assembly with the Differential Die-away Method Within the Scope of the Next Generation Safeguards Initiative Spent Fuel Project," *Journals of Nuclear Materials Management,* vol. 40, no. 3, pp. 61-69, 2012.

[7] D. Hartanto, J. Hu and R. McElroy Jr., "Conceptual Design and Analysis of Neutron Detectors for Safeguards Measurements of an Irradiated Pebble," Oak Ridge National Laboratory, ORNL/SPR-2024/3661, Oak Ridge, TN, 2024.

[8] R. D. McElroy and A. Lousteau, "Design of a Very High-Performance Neutron Multiplicity Counter (VPMC)," ORNL, ORNL/SPR-2023/2904, Oak Ridge, 2023.

[9] C. J. Werner (ed.), "MCNP User's Manual Code Version 6.2," LA-UR-17-29981, Los Alamos National Laboratory, NM, USA, 2017.

[10] J. Stempien et al., "AGR-2 TRISO Fuel Post-Irradiation Examination Final Report," Idaho National Laboratory, INL/EXT-21-64279, September 2021.

[11] B. Pham et al., "AGR-5/6/7 Irradiation Test Final As-run Report," Idaho National Laboratory, INL/EXT-21-64221-Rev000, Idaho Falls, ID, 2021.

[12] J. W. Sterbentz, "ECAR-2066 JMOCUP As-Run Daily Depletion Calculation for the AGR-2 Experiment in ATR B-12 Position," Idaho National Laboratory, INL/MIS-23-71642-Revision-0, Idaho Falls, ID, 2014.

[13] J. Sterbentz, "JMOCUP Physics Depletion Calculations for the As-Run AGR-5/6/7 TRISO Particle Experiment in ATR Northeast Flux Trap," Idaho National Laboratory, INL/MIS-20-60700-Revision-0, Idaho Falls, ID, 2020.

[14] A. Le Coq et al., "UCO TRISO MiniFuel FY23 NSUF-Kairos Power Post-Irradiation Examination Status Report," Oak Ridge National Laboratory, ORNL/TM-2023/2985, August 2023.

[15] K. Goetz et al., "Investigation of Coincidence Counting for Improving Minimal Detectable Activity of 110mAg in Single Particle Gamma Analysis," Oak Ridge National Laboratory, ORNL/TM--2023/2875, https://doi.org/10.2172/1968679, Oak Ridge, TN, 2023.

[16] H3D, "H3D M400 Spec Sheet," [Online]. Available: https://h3dgamma.com/M400Specs.pdf.

[17] IAEA, "Development and Implementation Support Programme for Nuclear Verification 2024–2025," [Online]. Available: https://www.iaea.org/sites/default/files/24/01/development-and-implementation-support-programme-for-nucear-verification-2024-2025.pdf.

[18] J. Hu et al., "Developing Spent Fuel Assembly for Advanced NDA Instrument Calibration - NGSI Spent Fuel Project," ORNL, https://doi.org/10.2172/1122693, Oak Ridge, TN, 2014.

[19] *Private communications with Bihn Pham at INL,* 2025.